

**Active Control of Resiliently-Mounted Beams
using Triangular Actuators**

Chinsuk Hong, Paolo Gardonio and Stephen J. Elliott

ISVR Technical Report N° 05/306

December 2005



SCIENTIFIC PUBLICATIONS BY THE ISVR

Technical Reports are published to promote timely dissemination of research results by ISVR personnel. This medium permits more detailed presentation than is usually acceptable for scientific journals. Responsibility for both the content and any opinions expressed rests entirely with the author(s).

Technical Memoranda are produced to enable the early or preliminary release of information by ISVR personnel where such release is deemed to be appropriate. Information contained in these memoranda may be incomplete, or form part of a continuing programme; this should be borne in mind when using or quoting from these documents.

Contract Reports are produced to record the results of scientific work carried out for sponsors, under contract. The ISVR treats these reports as confidential to sponsors and does not make them available for general circulation. Individual sponsors may, however, authorize subsequent release of the material.

COPYRIGHT NOTICE

(c) ISVR University of Southampton All rights reserved.

ISVR authorises you to view and download the Materials at this Web site ("Site") only for your personal, non-commercial use. This authorization is not a transfer of title in the Materials and copies of the Materials and is subject to the following restrictions: 1) you must retain, on all copies of the Materials downloaded, all copyright and other proprietary notices contained in the Materials; 2) you may not modify the Materials in any way or reproduce or publicly display, perform, or distribute or otherwise use them for any public or commercial purpose; and 3) you must not transfer the Materials to any other person unless you give them notice of, and they agree to accept, the obligations arising under these terms and conditions of use. You agree to abide by all additional restrictions displayed on the Site as it may be updated from time to time. This Site, including all Materials, is protected by worldwide copyright laws and treaty provisions. You agree to comply with all copyright laws worldwide in your use of this Site and to prevent any unauthorised copying of the Materials.

UNIVERSITY OF SOUTHAMPTON
INSTITUTE OF SOUND AND VIBRATION RESEARCH
SIGNAL PROCESSING & CONTROL GROUP

Active Control of Resiliently-Mounted Beams using Triangular Actuators

by

Chinsuk Hong, Paolo Gardonio and Stephen J. Elliott

ISVR Technical Report N° 05/306

December 2005

Authorised for issue by
Prof R Allen
Group Chairman

ABSTRACT

This report is concerned with triangularly-shaped actuators for the implementation of direct velocity feedback control(DVFC) systems. From the general theory of the piezo-ceramic actuator, the resultant actuation due to triangularly-shaped piezo-patch are derived. The dynamic response of resiliently-mounted beam supported with both rotational and linear springs at both ends is presented and the direct velocity feedback control of the beam using the triangularly-shaped piezoceramic actuator positioned at either ends of the beam is then studied.

It is found that the control system is influenced by the boundary condition of the beam as well as the shape of the actuator. When the beam is clamped at both ends, the triangularly-shaped actuator generates a force actuation which is perfectly collocated and dual with a velocity sensor at the tip of the triangular actuator so that the control system is unconditionally stable. In terms of control performance, however, the control system for a simply-supported beam is better than that for the clamped beam although the system is only conditionally stable. For practical boundary conditions achieved by the combination of the rotational and linear springs, the linear spring is the essential component necessary to achieve effectively collocated actuation in a desired frequency range, while the rotational spring is not effective.

The effect of the shape of the actuator is finally investigated. The bigger top angle the actuator has, the bigger the plant responds. With wide angled triangularly-shaped piezoactuator, hence the control effort can be saved. Another factor to be considered is the effect of height of the actuator. The larger height of actuator, the larger in amplitude of plant response can be obtained. The control effort can then be lowered with a larger height of actuator. The two factors, the top angle and the height, are however dependent variable such that the top angle is decreased when the height is increased. Another effect of the height is that the frequency range where stability is guaranteed is decreased as the height increases. It is necessary, therefore, to find the optimal dimension of the actuator for the given beam in order to maximise the control performance in the frequency range of interest.

Contents

| | |
|--|-----------|
| List of Figures | v |
| List of Tables | ix |
| 1 Introduction | 2 |
| 2 Actuation Resultant due to Triangularly-Shaped Piezoelectric Actuator | 4 |
| 3 Triangularly-Shaped Actuator on Beams | 11 |
| 3.1 Governing Equation and Boundary Conditions | 11 |
| 3.2 Dynamic Characteristics of Free Vibration | 12 |
| 3.3 Equivalent Actuation Resultant for Beams | 22 |
| 3.4 Beam Response to Triangular Actuator Excitation | 26 |
| 4 DVFC for Beams using a Triangular Actuator | 27 |
| 4.1 Formulation | 27 |
| 4.2 Plant Response and Stability | 29 |

| | |
|---|-----------|
| <i>Contents</i> | iv |
| 4.2.1 Effect of the Boundary Condition | 29 |
| 4.2.2 Effect of the Actuator Shape | 43 |
| 4.3 Performance | 53 |
| 5 Conclusions | 63 |
| Appendix | 65 |
| A Response, Kinetic Energy and Radiated Sound Power of Beams | 65 |
| References | 69 |

List of Figures

| | | |
|-----|---|----|
| 2.1 | Thin flat plate with an arbitrary shaped piezoelectric actuator. | 6 |
| 2.2 | A general distribution function in two-dimensional space. | 7 |
| 2.3 | Triangularly-shaped piezoelectric distribution | 8 |
| 2.4 | Results of the piezoelectric operator acting on triangularly-shaped distribution | 9 |
| 2.5 | Variation of actuation with the actuator angle | 9 |
| 3.1 | Bernoulli-Euler beam with a general boundary condition, subject to force and moment actuation | 12 |
| 3.2 | Variation of natural frequencies with the linear spring constant, κ | 17 |
| 3.3 | Variation of natural frequencies with the rotational spring constant, τ . | 18 |
| 3.4 | Variation of mode shape with the linear spring constant when $\tau = 0$. . | 19 |
| 3.5 | Variation of mode shape with the rotational spring constant when $\kappa = 10^4$ | 20 |
| 3.6 | Variation of mode shape with the rotational spring constant when $\kappa = 10^6$ | 21 |
| 3.7 | Result of Laplacian of one dimensional transducer distribution | 22 |

| | | |
|------|---|----|
| 3.8 | Actuation for beams due to the triangularly-shaped actuator obtained from two dimensional approach. Note that the expressions in the figure are the resultant of the Laplacian operator so that the moments and forces generated are calculated multiplying $h_s v_{cs}(t)/2$ | 24 |
| 3.9 | Equivalent actuation resultant for beams having a distributed moment term | 24 |
| 3.10 | Equivalent actuation resultant for beams with concentrated actuation. Note that the expressions in the figure are the resultant of the Laplacian operator so that the moments and forces generated are calculated multiplying $h_s v_{cs}(t)/2$ | 25 |
| 4.1 | Active feedback control system using a triangular-shaped piezoceramic actuator | 28 |
| 4.2 | Plant response for a clamped beam from the triangularly-shaped piezoceramic actuator to the velocity sensor at $x = a$ | 31 |
| 4.3 | Plant response for a simply-supported beam from the triangularly-shaped piezoceramic actuator to the velocity sensor at $x = a$ | 33 |
| 4.4 | Components of the plant response for a simply-supported beam from the triangularly-shaped piezoceramic actuator to the velocity sensor at $x = a$; (a) due to collocated forces at $x = a$ and (b) due to moment $x = 0$ | 34 |
| 4.5 | Variation of the sign of the modal coupling factor with the mode index, n , and the shape of the piezoceramic actuator, θ_{PZT} . The white region denotes stable modes and the black region unstable. | 35 |
| 4.6 | Variation with the rotational spring constant at both ends in the bode diagram of the plant response for a simply-supported beam from the triangularly-shaped piezoceramic actuator to the velocity sensor at $x = a$ | 36 |
| 4.7 | Variation with the rotational spring constant at both ends in the Nyquist plot of the plant response for a simply-supported beam from the triangularly-shaped piezoceramic actuator to the velocity sensor at $x = a$ | 37 |

| | | |
|------|---|----|
| 4.8 | Boundary condition to investigate the effect of the linear spring on the stability of the control system. | 38 |
| 4.9 | Plant response for beams with the boundary condition $\tau = \infty$ and $\kappa = 0$ from the triangularly-shaped piezoceramic actuator to the velocity sensor at $x = a$ | 39 |
| 4.10 | Components of the plant response for beams with the boundary condition $\tau = \infty$ and $\kappa = 0$ from the triangularly-shaped piezoceramic actuator to the velocity sensor at $x = a$ | 40 |
| 4.11 | Variation with the linear spring constant in the bode diagram of the plant response for beams with the boundary condition $\tau = \infty$ at both ends from the triangularly-shaped piezoceramic actuator to the velocity sensor at $x = a$ | 41 |
| 4.12 | Variation with the linear spring constant in the Nyquist plot of the plant response for beams with the boundary condition $\tau = \infty$ at both ends from the triangularly-shaped piezoceramic actuator to the velocity sensor at $x = a$ | 42 |
| 4.13 | Maximum gain, maximum plant response and performance index with respect to the spring constants | 44 |
| 4.14 | Actuator shapes varied with the top angles of $\theta_{PZT} = 15^\circ, 30^\circ, 45^\circ, 60^\circ, 75^\circ$. The boundary condition of the beam is that $\kappa = 10^5$ and $\tau = 0$ | 45 |
| 4.15 | Variation of the plant response with the top angles of the triangularly-shaped piezoceramic actuator. The boundary condition of the beam is that $\kappa = 10^5$ and $\tau = 0$ | 46 |
| 4.16 | Variation of the performance index with top angles of the triangularly-shaped piezoceramic actuator. The boundary condition of the beam is that $\kappa = 10^5$ and $\tau = 0$ | 47 |
| 4.17 | Three different sizes of the actuators with the same shapes having $\theta_{PZT} = 37^\circ$ and the height of 5mm, 10mm and 20mm. The boundary condition of the beam is that $\kappa = 10^5$ and $\tau = 0$ | 47 |

| | | |
|------|---|----|
| 4.18 | Variation of the plant response with the sizes of the triangularly-shaped piezoceramic actuator. The boundary condition of the beam is that $\kappa = 10^5$ and $\tau = 0$ | 48 |
| 4.19 | Variation of the performance index with the size of the triangularly-shaped piezoceramic actuator. The boundary condition of the beam is that $\kappa = 10^5$ and $\tau = 0$ | 49 |
| 4.20 | Four different shapes of the actuators having $a = 20\text{mm}$, 50mm , 100mm and 200mm with the same base of 30mm | 50 |
| 4.21 | Variation of the plant response with the size of the triangularly-shaped piezoceramic actuator. The boundary condition of the beam is that $\kappa = 10^5$ and $\tau = 0$ | 51 |
| 4.22 | Variation of the performance index with the size of the triangularly-shaped piezoceramic actuator. The boundary condition of the beam is that $\kappa = 10^5$ and $\tau = 0$ | 52 |
| 4.23 | Control performance of direct velocity feedback control of a clamped beam using a triangularly-shaped piezoceramic actuator($a=25\text{mm}$, $b=15\text{mm}$) with the feedback gains of 10^3 , 10^4 and 10^5 | 54 |
| 4.24 | Control performance of direct velocity feedback control of a simply supported beam using a triangularly-shaped piezoceramic actuator($a=25\text{mm}$, $b=15\text{mm}$) with the feedback gains of 10^2 , 10^3 and 2×10^3 | 55 |
| 4.25 | Control performance of direct velocity feedback control of a resiliently-mounted($\kappa = 10^5$ and $\tau = 0$) beam using a triangularly-shaped piezoceramic actuator($a=25\text{mm}$, $b=15\text{mm}$) with the feedback gains of 100, 300 and 600. | 56 |
| 4.26 | Variation of the normalised control performance, integrated up to 2kHz , with the feedback gain from 1 to 10^6 for clamped beam(solid line), simply-supported beam(dot-dashed line) and resiliently-mounted beam($\kappa = 10^5$ and $\tau = 0$)(dashed line), of beams using a triangularly-shaped piezoceramic actuator($a=25\text{mm}$, $b=15\text{mm}$) | 58 |

-
- 4.27 Effect of the actuator's top angle on the normalised control performance with the feedback gain from 0.1 to 10^4 for the resiliently-mounted ($\kappa = 10^5$ and $\tau = 0$) beam using a triangularly-shaped piezoceramic actuator with $b=15\text{mm}$ and $\theta_{PZT} = 15^\circ$ (thick solid), $\theta_{PZT} = 30^\circ$ (dotted), $\theta_{PZT} = 45^\circ$ (dot-dashed), $\theta_{PZT} = 60^\circ$ (dashed), $\theta_{PZT} = 75^\circ$ (solid). . . . 59
- 4.28 Effect of the actuator shape on the normalised control performance with the feedback gain from 0.1 to 10^4 for the resiliently-mounted ($\kappa = 10^5$ and $\tau = 0$) beam using a triangularly-shaped piezoceramic actuator with $\theta_{PZT} = 37^\circ$ and $a=5\text{mm}$ (solid), 10mm (dashed) and 20mm (dotted). 60
- 4.29 Effect of the actuator shape on the normalised control performance with the feedback gain from 0.1 to 10^4 for the resiliently-mounted ($\kappa = 10^5$ and $\tau = 0$) beam using a triangularly-shaped piezoceramic actuator with $b=15\text{mm}$ and $a=20\text{mm}$ (solid), 50mm (dashed), 100mm (dotted) and 200mm (dot-dashed). 62

List of Tables

| | | |
|-----|---|----|
| 2.1 | Geometry and physical parameters for the piezoelectric actuator | 10 |
| 3.1 | Mechanical properties and masses | 16 |

Chapter 1

Introduction

Control of the low-frequency sound transmission through a lightly damped and lightweight panel in aircrafts, space vehicles, automobiles and underwater vehicles is an important design issue. The sound transmission at low frequencies can be reduced by controlling the response of the panel itself and by modifying the radiation efficiency of the low frequency resonant modes[1]. It is hence necessary to stiffen the panel in order to increase the first few natural frequencies, or to apply damping materials to the panel in order to reduce the response at the resonant frequencies. These passive techniques have a limited performance at the low frequencies and require substantial variation to the structure of the panel causing several drawbacks such as the change of geometry and weight and the increase of costs[2]. Alternatively, active control techniques could be employed where sensor/actuator transducers governed by an active controller used. There are two main kinds of actuators for this structure: force actuators and strain actuators. Using point velocity sensors the force actuators can easily form a collocated and dual sensor-actuator pairs which is particularly convenient for the implementation of direct velocity feedback control schemes that enables the control of broadband random disturbances. However, this configuration tends to be heavy and occupy large volumes. To achieve compact and light weight smart panels, strain actuators have been considered. Normally arrays of square piezoelectric patch actuators with accelerometer sensor at their centre are used[3–6]. This configuration, however, has a difficulty to ensure unconditionally stable feedback loop because the sensor-actuator pair is not truly collocated and dual. Furthermore, the actuation resultant obtained from the piezo-patch is a distribution of moments along the edges which more effectively couples into higher modes of the structure so that the gain margin is relatively low.

Recently Gardonio and Elliott[2] have proposed to use triangularly-shaped piezo-actuators

arranged along the perimeter of the radiating structure with accelerometers at their top vertexes. In this context they found that the configuration gives much larger gain margin and better performance than using the square patches. Since in practice the boundary condition is not perfectly simply supported condition, more understanding about the force and moments generated by the triangularly-shaped piezoceramic actuator on a structure with compliant boundaries is required.

In this study, based on the formulation of a generally-distributed piezoceramic patch[7, 8], the actuation resultant due to a triangularly-shaped piezoceramic actuator is derived in Chapter 2. The application of the resultant actuation to a beam model is then presented in Chapter 3. Using the formulations derived in Chapters 2 and 3, a direct velocity feedback control system for beams using the triangularly-shaped actuator is studied in Chapter 4, in order to find the effect of the boundary condition encountered in practice and the shape of the actuators on the stability and the performance of the control system. Finally conclusions are summarised in Chapter 5.

Chapter 2

Actuation Resultant due to Triangularly-Shaped Piezoelectric Actuator

The excitation due to the piezoelectric actuator results from the elastic coupling of the actuator and the structure on which it is attached. Assuming first-order shear deformation[7, 9] in the structure, the governing equations of laminated piezoelectric plates has been derived by Lee[7], from which it is known that the actuation due to the piezoelectric actuator is expressed with the spatial differential operator of an strain induced transducer, e.g., piezoelectric actuator, as follow¹;

$$L[\Lambda(x, y)] = e_{31}^0 \frac{\partial^2 \Lambda(x, y)}{\partial^2 x} + e_{32}^0 \frac{\partial^2 \Lambda(x, y)}{\partial^2 y} + 2e_{36}^0 \frac{\partial^2 \Lambda(x, y)}{\partial x \partial y} \quad (2.1)$$

where $\Lambda(x, y)$ is the distribution function describing the shape of the piezoelectric actuator² and e_{31}^0 , e_{32}^0 and e_{36}^0 represent the piezoelectric stress/charge constants with respect to the structure axes. When the *skew angle* between the transducer and the structure axes is θ , they can be estimated by

$$\mathbf{e} = \mathbf{T}^{-1}(\theta) \mathbf{C} \mathbf{d}' \quad (2.2)$$

where \mathbf{e} is the vector form of the piezoelectric stress/charge constants, $\mathbf{e} = \{e_{31}^0 \ e_{32}^0 \ e_{36}^0\}^T$, \mathbf{T} is the stress tensor transformation matrix[7] from the structure axes to the piezo-

¹The coefficient 2 in the last term does not appear in ref [10]

²Strictly speaking, this function denotes the shape of the electrode on the piezoelectric actuator. In this case, however, they are the same.

material axes. The inverse transformation is then

$$\mathbf{T}^{-1}(\theta) = \begin{bmatrix} \cos^2 \theta & \sin^2 \theta & -2 \cos \theta \sin \theta \\ \sin^2 \theta & \cos^2 \theta & 2 \cos \theta \sin \theta \\ \cos \theta \sin \theta & -\cos \theta \sin \theta & \cos^2 \theta - \sin^2 \theta \end{bmatrix} \quad (2.3)$$

\mathbf{C} is the stiffness matrix of the piezoelectric actuator;

$$\mathbf{C} = \begin{bmatrix} \frac{Y_{PZT}}{1 - \nu_{PZT}^2} & \frac{\nu_{PZT} Y_{PZT}}{1 - \nu_{PZT}^2} & 0 \\ \frac{\nu_{PZT} Y_{PZT}}{1 - \nu_{PZT}^2} & \frac{Y_{PZT}}{1 - \nu_{PZT}^2} & 0 \\ 0 & 0 & \frac{Y_{PZT}}{2(1 + \nu_{PZT})} \end{bmatrix}, \quad (2.4)$$

where Y_{PZT} and ν are Young's modulus and Poisson's ratio, respectively, of the piezoelectric actuator, and \mathbf{d}' is the vector form of the piezoelectric strain/charge constants with respect to the piezo-material axes so that $\mathbf{d}' = \{d_{3'1'}^0, d_{3'2'}^0, 0\}^T$.

Assuming that the plate is very thin, isotropic and homogeneous and the passive effects of the piezoelectric actuator are neglected, the governing equation for a flat plate with a piezoelectric actuator of an arbitrary shape as shown in Figure 2.1 can be written as

$$D_{11} \left(\frac{\partial^4 w}{\partial x^4} + 2 \frac{\partial^4 w}{\partial^2 x \partial^2 y} + \frac{\partial^4 w}{\partial^4 y} \right) + \rho h \frac{\partial^2 w}{\partial t^2} = q(x, y, t) + \frac{h_s}{2} L[\Lambda(x, y)] v_{cs}(t) \quad (2.5)$$

where $D_{11} = \frac{Y_p h_p^3}{12(1-\nu^2)}$ is the bending rigidity, w is the transverse displacement of the plate, ρ is the density, h is the thickness of the plate, $q(x, y, t)$ is an externally applied excitation, $v_{cs}(t)$ is the applied voltage to the piezoelectric actuator, and $h_s = h_p + h_{PZT}$ in which h_{PZT} is the thickness of the piezoelectric actuator.

Generalised functions can be used to describe the distribution of the transducer. The generalised functions can conveniently be dealt with the Macauley notation[10]. For instance, $\langle x - a \rangle^0$ represents a step function, $h(x - a)$, which begins at $x = a$. The derivative with respect to x of the step function is given by $\langle x - a \rangle^{-1}$ which is the delta function at $x = a$, i.e, $\delta(x - a)$. The derivative of this delta function yields $\langle x - a \rangle^{-2}$, a doublet function at $x = a$, i.e, $\delta'(x - a)$. The integral of the step function with respect to x yields a ramp function, $\langle x - a \rangle^1$, which is zero up to $x = a$ and then is equal to $x - a$. Using the characteristics of the multidimensional general functions that can be expressed by the product of one dimensional generalised function of each direction, the distribution function can be defined. For example, the

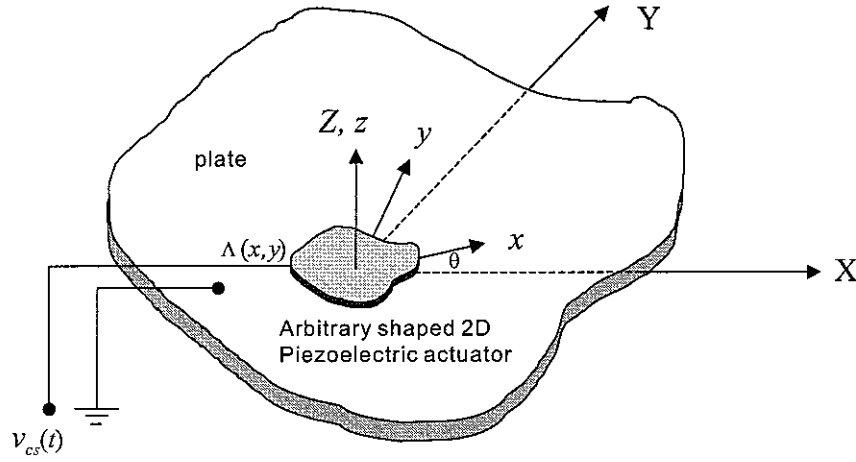


Figure 2.1: Thin flat plate with an arbitrary shaped piezoelectric actuator.

region of two-dimensional distribution shown in Figure 2.2 can be described by

$$\begin{aligned} y &= f_1(x), \quad \text{for } y > 0 \text{ over } x \in [x_2, x_1] \\ y &= f_2(x), \quad \text{for } y < 0 \text{ over } x \in [x_2, x_1] \end{aligned} \quad (2.6)$$

where x_1 and x_2 are the x extrema of the boundary. This distribution can be described using the generalised function and the characteristics as follow;

$$\Lambda(x, y) = (\langle x - x_2 \rangle^0 - \langle x - x_1 \rangle^0) (\langle y - f_2(x) \rangle^0 - \langle y - f_1(x) \rangle^0) \quad (2.7)$$

Within the boundary, the distribution has unit amplitude, $\Lambda = 1$, and outside of the boundary it has zero amplitude, $\Lambda = 0$. Equation 2.7 can be used to describe a two-dimensional distributed transducer of arbitrary shape.

The spatial distribution defined in Equation 2.7 is a product of two terms one of which is solely dependent on x and the other of which is dependent on both x and y , so that

$$\Lambda(x, y) = \Lambda_1(x)\Lambda_2(x, y). \quad (2.8)$$

and the partial derivatives of this distribution function with respect to x and y can be expressed as

$$\frac{\partial \Lambda(x, y)}{\partial x} = \Lambda_1'(x)\Lambda_2(x, y) + \Lambda_1(x)\frac{\partial \Lambda_2(x, y)}{\partial x}, \quad (2.9)$$

and

$$\frac{\partial \Lambda(x, y)}{\partial y} = \Lambda_1(x)\frac{\partial \Lambda_2(x, y)}{\partial y}. \quad (2.10)$$

Taking higher-order spatial derivatives of the function successively to Equations 2.9

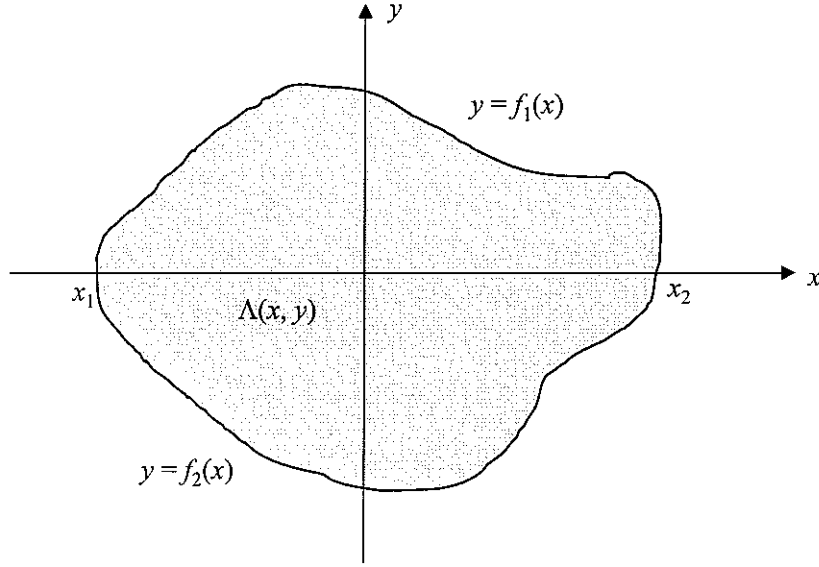


Figure 2.2: A general distribution function in two-dimensional space.

and 2.10, one can obtain the derivatives in Equation 2.1.

$$\frac{\partial^2 \Lambda(x, y)}{\partial x \partial y} = \Lambda_1'(x) \frac{\partial \Lambda_2(x, y)}{\partial y} + \Lambda_1(x) \frac{\partial^2 \Lambda_2(x, y)}{\partial x \partial y}, \quad (2.11)$$

and

$$\frac{\partial^2 \Lambda(x, y)}{\partial x^2} = \Lambda_1(x)'' \Lambda(x, y) + 2\Lambda_1'(x) \frac{\partial \Lambda_2(x, y)}{\partial x} + \Lambda_1(x) \frac{\partial^2 \Lambda_2(x, y)}{\partial x^2} \quad (2.12)$$

and

$$\frac{\partial^2 \Lambda(x, y)}{\partial y^2} = \Lambda_1(x) \frac{\partial^2 \Lambda_2(x, y)}{\partial y^2}. \quad (2.13)$$

Substituting Equation 2.7 into Equations 2.11 to 2.13, one can obtain an explicit expressions for the Laplacian of the distribution function in terms of the generalised functions. The derivatives of the distribution function can be worked out using the spatial distributional chain rule[10].

Now, consider the triangularly-shaped piezoelectric distribution shown in Figure 2.3. The shape can be described by Equation 2.7, where $f_1(x) = -mx + b$ and $f_2(x) = mx - b$;

$$\Lambda(x, y) = (\langle x \rangle^0 - \langle x - a \rangle^0) (\langle y - mx + b \rangle^0 - \langle y + mx - b \rangle^0) \quad (2.14)$$

Assuming that the distribution of the piezoelectric actuator on the plate is represented by the coordinate system coincident with the material coordinates (skew angle $\theta = 0$), one can obtain the result of the piezoelectric operator, $L[\Lambda(x, y)]$. Substituting

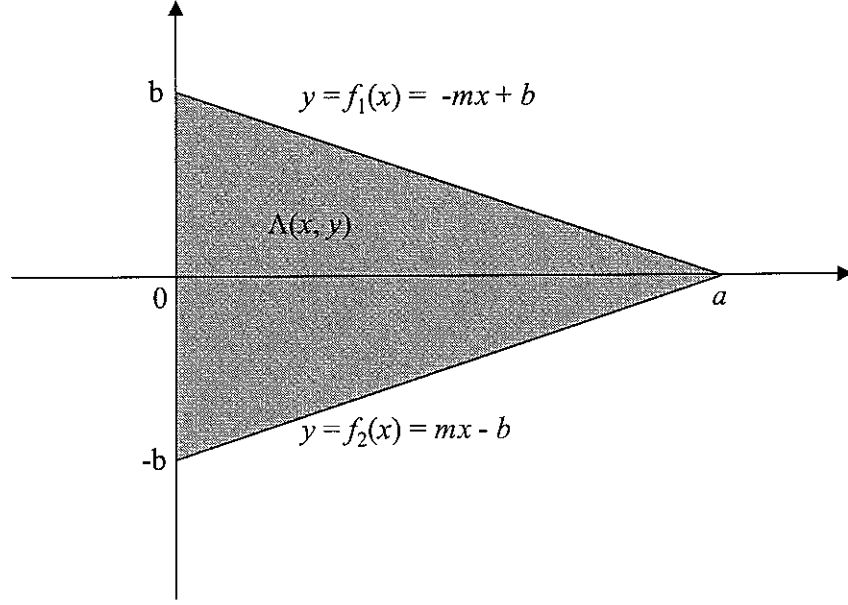


Figure 2.3: Triangularly-shaped piezoelectric distribution

Equation 2.14 into Equations 2.11, 2.12 and 2.13 leads to

$$\begin{aligned}
 L[\Lambda(x, y)] &= e_{31}^0 (\langle x \rangle^{-2} - \langle x - a \rangle^{-2}) \\
 &\quad \times (\langle y - mx + b \rangle^0 - \langle y + mx - b \rangle^0) \\
 &- 2me_{31}^0 (\langle x \rangle^{-1} - \langle x - a \rangle^{-1}) \\
 &\quad \times (\langle y - mx + b \rangle^{-1} - \langle y + mx - b \rangle^{-1}) \\
 &+ (m^2 e_{31}^0 + e_{32}^0) (\langle x \rangle^0 - \langle x - a \rangle^0) \\
 &\quad \times (\langle y - mx + b \rangle^{-2} - \langle y + mx - b \rangle^{-2}).
 \end{aligned} \tag{2.15}$$

The physical interpretation of Equation 2.15 can be clearly addressed following the reference[10]. The first term in Equation 2.15 denotes the distribution of doublet functions of magnitude e_{31}^0 on the lines $x = 0$ and $x = a$, but only between the lines $y = mx - b$ and $y = -mx + b$. Thus there is no distributed doublets on the line $x = a$ because the sloped lines intersect at $x = a$ so that no boundary exists. The third term in Equation 2.15 denotes the distributed doublets of magnitude $m^2 e_{31}^0 + e_{32}^0$, on the lines $y = mx - b$ and $y = -mx + b$, but between $x = 0$ and $x = a$. The second term in Equation 2.15 expresses the delta functions of magnitude of $2me_{31}^0$ acting downwardly at the points $(0, b)$ and $(0, -b)$ and of $4me_{31}^0$ acting upwardly at the points $(a, 0)$. Figure 2.4 depicts the results of the actuation operator generated by a triangularly-shaped piezoelectric actuator.

Equations 2.5 and 2.15 show that, for a given piezoelectric material bonded on a plate

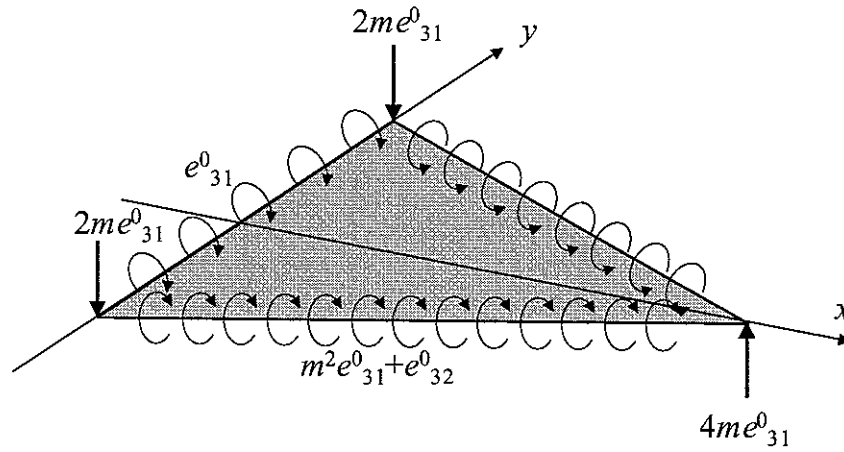


Figure 2.4: Results of the piezoelectric operator acting on triangularly-shaped distribution

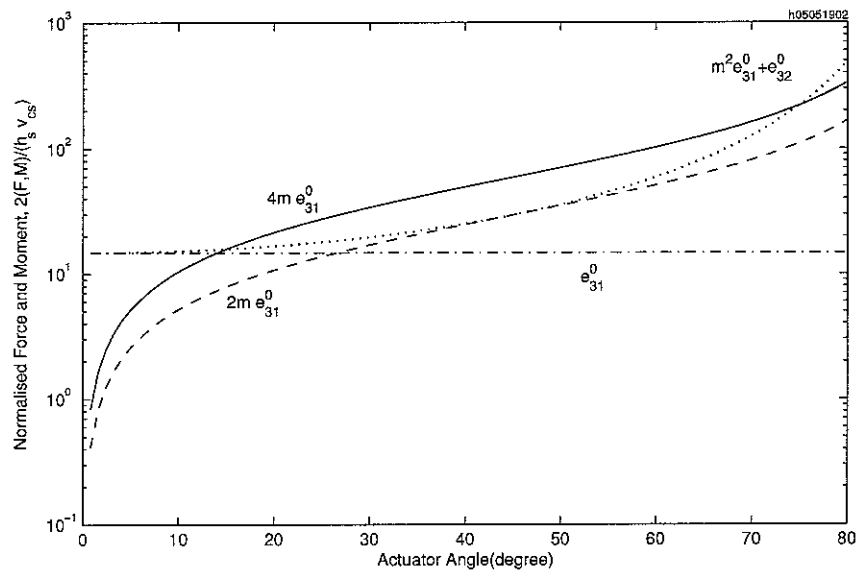


Figure 2.5: Variation of actuation with the actuator angle

Table 2.1: Geometry and physical parameters for the piezoelectric actuator

| Parameters | Symbol | Unit | Values |
|---------------------------------------|--------------|-------------------|-----------------------|
| Thickness | h_{PZT} | mm | 1.0 |
| Young's modulus | Y_{PZT} | GPa | 63 |
| Density | ρ_{PZT} | kg/m ³ | 7600 |
| Poisson ratio | ν_{PZT} | | 0.29 |
| Piezoelectric stress/charge constants | $d_{3'1'}^0$ | V/m(or C/N) | 166×10^{-12} |
| | $d_{3'2'}^0$ | V/m(or C/N) | 166×10^{-12} |
| | $d_{3'6'}^0$ | V/m(or C/N) | 0 |

with skew angle $\theta = 0$, the magnitude of actuation depends on the thickness of the piezoelectric actuator (h_{PZT}), the thickness of the plate (h_p) on which the actuator is attached, and the shape of actuator ($m = b/a = \tan \theta_{PZT}$). Figure 2.5 shows their dependence on the shape of actuator. Table 2.1 shows geometry and physical parameters for the piezoelectric actuator used in the calculation. While the moment on the side along the y axes is constant, the other forces and moments strongly depend on the shape of the actuator. The excitation effectiveness of the actuator bonded on a structure, however, depends on the coupling of the excitation field with the modal response of the structure, rather than the absolute value of the actuation. The effectiveness of the force generated to the response of the structure is directly related to the modal displacement at the force location while that of the moment is related to the slope of the mode at the moment location.

Chapter 3

Triangularly-Shaped Actuator on Beams

3.1 Governing Equation and Boundary Conditions

Consider a beam supported on springs as shown in Figure 3.1. The beam is subjected to forces and moments along the length. Assuming it behaves as the Euler-Bernoulli beam, the equation of motion for the forced lateral vibration of a uniform beam is obtained [11, 12]:

$$\mathcal{L}_b(w; x, t) = f(x, t) + \frac{\partial T}{\partial x}(x, t), \quad (3.1)$$

where $f(x, t)$ and $T(x, t)$ are the external force and moment per unit length of the beam, respectively, and $\mathcal{L}_b(w; x, t)$ is the beam dynamic operator expressed as

$$\mathcal{L}_b(w; x, t) = E(1 + j\eta)I \frac{\partial^4 w}{\partial x^4}(x, t) + \rho A \frac{\partial^2 w}{\partial t^2}(x, t), \quad (3.2)$$

where E is Young's modulus, I is the moment of inertia of the beam cross section about the y axis, η is loss factor, ρ is mass density and A is cross sectional area of the beam. For the harmonic motion as $w(x, t) = W(x, \omega)e^{j\omega t}$, Equation 3.2 can be written as

$$\mathcal{L}_b(w; x, \omega) = E(1 + j\eta)I \frac{\partial^4 W}{\partial x^4}(x, \omega) - \rho A \omega^2 W(x, \omega). \quad (3.3)$$

Since the triangularly-shaped actuator generates forces and moments, they are included in the model shown in Figure 3.1. A general boundary condition can be represented

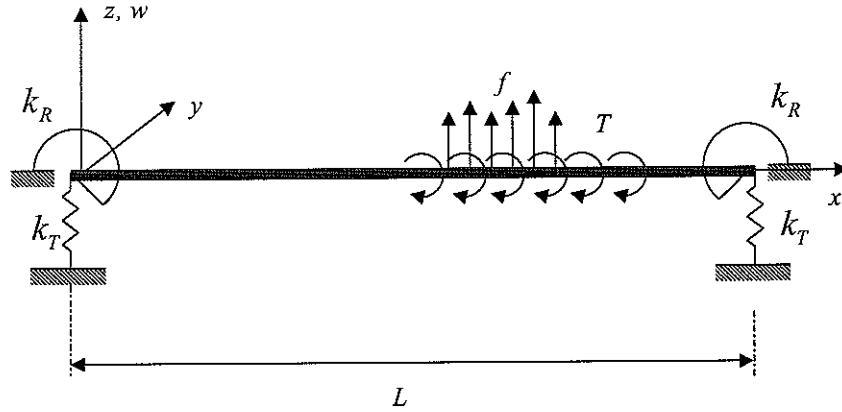


Figure 3.1: Bernoulli-Euler beam with a general boundary condition, subject to force and moment actuation

with a rotational spring and a linear spring at each end of the beam. The boundary conditions resulting from the configurations are given by the moment and shear force balance at the ends. Hence, the boundary conditions are, at $x = 0$,

$$\frac{\partial^2 w}{\partial x^2} = \frac{k_R}{EI} \frac{\partial w}{\partial x}, \quad \frac{\partial^3 w}{\partial x^3} = -\frac{k_T}{EI} w \quad (3.4)$$

and at $x = L$

$$\frac{\partial^2 w}{\partial x^2} = -\frac{k_R}{EI} \frac{\partial w}{\partial x}, \quad \frac{\partial^3 w}{\partial x^3} = \frac{k_T}{EI} w \quad (3.5)$$

where k_R and k_T are the linear and rotational spring constants, respectively.

3.2 Dynamic Characteristics of Free Vibration

Consider the homogeneous equation of Equation (3.1) expressed as

$$EI \frac{\partial^4 w}{\partial x^4}(x, t) + \rho A \frac{\partial^2 w}{\partial t^2}(x, t) = 0. \quad (3.6)$$

The first step toward obtaining a solution of Equation 3.6 is to assume the solution as a harmonic solution as shown Equation 3.7.

$$w(x, t) = \phi(x) e^{j\omega t}, \quad (3.7)$$

where $\phi(x)$ is a complex function of x alone. Upon substitution of Equation 3.7 into Equation 3.6, the exponential function of time cancels out, leaving new differential

equation as a function of x . The equation is expressed by

$$\frac{\partial^4 \phi(x)}{\partial x^4} - \beta^4 \phi(x) = 0. \quad (3.8)$$

where $\beta^4 = \omega^2 \frac{\rho A}{EI}$, i.e. $\beta = \pm \sqrt[4]{\frac{\rho A \omega^2}{EI}}$ or $\beta = \pm j \sqrt[4]{\frac{\rho A \omega^2}{EI}}$.

Taking spatial Laplace Transform of Equation 3.8 it is formed

$$(s^4 - \beta^4)\Phi(s) = s^3 \phi(0) + s^2 \phi'(0) + s \phi''(0) + \phi'''(0). \quad (3.9)$$

Solving for $\Phi(s)$ in Equation 3.9 and expanding the right-hand side by partial fractions yields

$$\begin{aligned} \Phi(s) &= \frac{1}{2} \left(\frac{s}{s^2 + \beta^2} + \frac{s}{s^2 - \beta^2} \right) \phi(0) \\ &+ \frac{1}{2} \left(\frac{1}{s^2 + \beta^2} + \frac{1}{s^2 - \beta^2} \right) \phi'(0) \\ &+ \frac{1}{2\beta^2} \left(\frac{-s}{s^2 + \beta^2} + \frac{s}{s^2 - \beta^2} \right) \phi''(0) \\ &+ \frac{1}{2\beta^2} \left(\frac{-1}{s^2 + \beta^2} + \frac{1}{s^2 - \beta^2} \right) \phi'''(0) \end{aligned} \quad (3.10)$$

The inverse transform of Equation 3.10 is

$$\begin{aligned} \phi(x) &= \phi(0)U(\beta x) + \phi'(0) \frac{V(\beta x)}{\beta} \\ &+ \phi''(0) \frac{S(\beta x)}{\beta^2} + \phi'''(0) \frac{T(\beta x)}{\beta^3} \end{aligned} \quad (3.11)$$

where

$$\begin{aligned} U(x) &= \frac{1}{2}(\cos x + \cosh x) \\ V(x) &= \frac{1}{2}(\sin x + \sinh x) \\ S(x) &= \frac{1}{2}(\cosh x - \cos x) \\ T(x) &= \frac{1}{2}(\sinh x - \sin x) \end{aligned} \quad (3.12)$$

Noting that $U(0)=1$, $V(0)=0$, $S(0)=0$, $T(0)=0$, $U'(\beta x) = \beta T(\beta x)$, $V'(\beta x) = \beta U(\beta x)$, $S'(\beta x) = \beta V(\beta x)$, and $T'(\beta x) = \beta S(\beta x)$, substituting the boundary conditions (3.4)

and (3.5) into Equation 3.11 yields the frequency characteristic equation as

$$\begin{aligned}
& [b_0 b_L (a_0 + a_L) + (b_0 - b_L)] (\cos \beta L \sinh \beta L + \sin \beta L \cosh \beta L) \\
& + [a_0 a_L (b_0 - b_L) - (a_0 + a_L)] (\cos \beta L \sinh \beta L - \sin \beta L \cosh \beta L) \quad (3.13) \\
& - 2(a_0 a_L - b_0 b_L) \sin \beta L \sinh \beta L + (1 - a_0 a_L b_0 b_L) (\cos \beta L \cosh \beta L - 1) \\
& + (a_L b_L - a_0 b_0) (\cos \beta \cosh \beta + 1) + 2(a_0 b_L - a_L b_0) \cos \beta \cosh \beta = 0
\end{aligned}$$

where

$$\begin{aligned}
a_0 &= \frac{k_L}{EI\beta^3} \\
a_L &= \frac{k_L}{EI\beta^3} \quad (3.14)
\end{aligned}$$

$$\begin{aligned}
b_0 &= \frac{k_R}{EI\beta} \\
b_L &= \frac{k_R}{EI\beta} \quad (3.15)
\end{aligned}$$

and it should be noted that a_0 , a_L , b_0 and b_L are function of β , when solving Equation 3.13. The roots of Equation 3.13, $\beta_n L$, give the natural frequencies of vibration from the Equation 3.16 as follow :

$$\omega_n = (\beta_n L)^2 \left(\frac{EI}{\rho A L^4} \right)^{1/2}, \quad n = 1, 2, 3, \dots \quad (3.16)$$

where the values of $\beta_n L$ satisfying Equation 3.13 are obtained numerically by using non-linear equation solving algorithm such as Newton's method. In order to avoid the singularity in $\phi_n(x)$, Equation 3.11 is written in four different forms.

When $0 \leq a_{0n} < \infty$ and $0 \leq b_{0n} < \infty$, the mode shape function is

$$\phi_n(x) = \varepsilon_n \left[C_n^{(1)} \{U(\beta_n x) - a_{0n} T(\beta_n x)\} + V(\beta_n x) + b_{Ln} S(\beta_n x) \right] \quad (3.17)$$

where

$$C_n^{(1)} = \frac{a_{Ln} V(\beta_n L) + (a_{Ln} b_{0n} - 1) S(\beta_n L) - b_{0n} T(\beta_n L)}{V(\beta_n L) - (a_{0n} + a_{Ln}) U(\beta_n L) + a_{0n} a_{Ln} T(\beta_n L)}. \quad (3.18)$$

When $0 < a_{Ln} \leq \infty$ and $0 \leq b_{Ln} < \infty$,

$$\phi_n(x) = \varepsilon_n \left[C_n^{(2)} \left\{ T(\beta_n x) - \frac{1}{a_{0n}} U(\beta_n x) \right\} + V(\beta_n x) + b_{0n} S(\beta_n x) \right] \quad (3.19)$$

where

$$C_n^{(2)} = \frac{a_{Ln}V(\beta_n L) - b_{0n}T(\beta_n L) + (a_{Ln}b_{0n} - 1)S(\beta_n L)}{[(a_{Ln}/a_{0n}) + 1]U(\beta_n L) - a_{Ln}T(\beta_n L) - (1/a_{0n})V(\beta_n L)}. \quad (3.20)$$

When $0 \leq a_{Ln} < \infty$ and $0 < b_{Ln} \leq \infty$,

$$\phi_n(x) = \varepsilon_n \left[C_n^{(3)} \{U(\beta_n x) - a_{0n}T(\beta_n x)\} + \frac{1}{b_{0n}}V(\beta_n x) + S(\beta_n x) \right] \quad (3.21)$$

where

$$C_n^{(3)} = \frac{(a_{Ln}/b_{0n})V(\beta_n L) - T(\beta_n L) + (a_{Ln} - 1/b_{0n})S(\beta_n L)}{V(\beta_n L) + a_{0n}a_{Ln}T(\beta_n L) - (a_{Ln} + a_{0n})U(\beta_n L)}. \quad (3.22)$$

When $0 < a_{Ln} \leq \infty$ and $0 \leq b_{Ln} < \infty$,

$$\phi_n(x) = \varepsilon_n \left[C_n^{(4)} \left\{ T(\beta_n x) - \frac{1}{a_{0n}}U(\beta_n x) \right\} + \frac{1}{b_{0n}}V(\beta_n x) + S(\beta_n x) \right] \quad (3.23)$$

where

$$C_n^{(4)} = \frac{(a_{Ln}/b_{0n})V(\beta_n L) - T(\beta_n L) + (a_{Ln} - 1/b_{0n})S(\beta_n L)}{[(a_{Ln}/a_{0n}) + 1]U(\beta_n L) - a_{Ln}T(\beta_n L) - (1/a_{0n})V(\beta_n L)}. \quad (3.24)$$

The constant ε_n shown in Equations 3.17, 3.19, 3.21 and 3.23 is a normalisation factor satisfying that

$$\frac{1}{L} \int_0^L \phi_n^2(x) dx = 1. \quad (3.25)$$

To examine the effect of the boundary condition on the dynamics, it is convenient to define non-dimensional spring constants for the linear spring constant,

$$\kappa = \frac{k_L L^3}{EI} \quad (3.26)$$

and for the torsional spring constant,

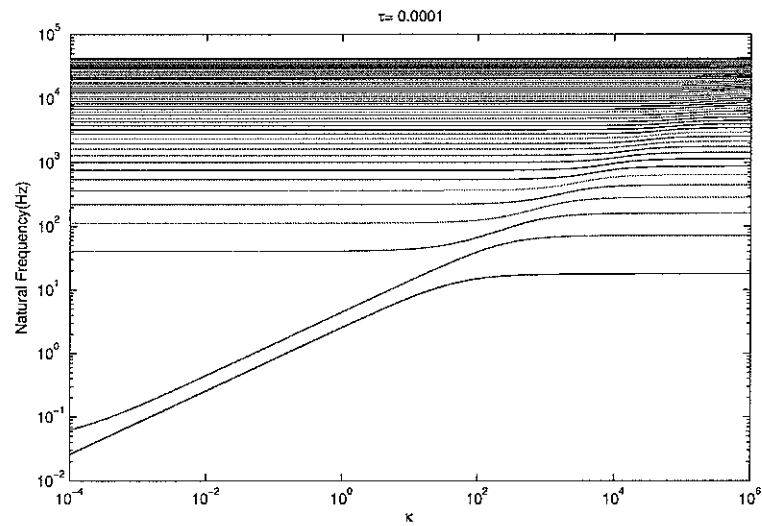
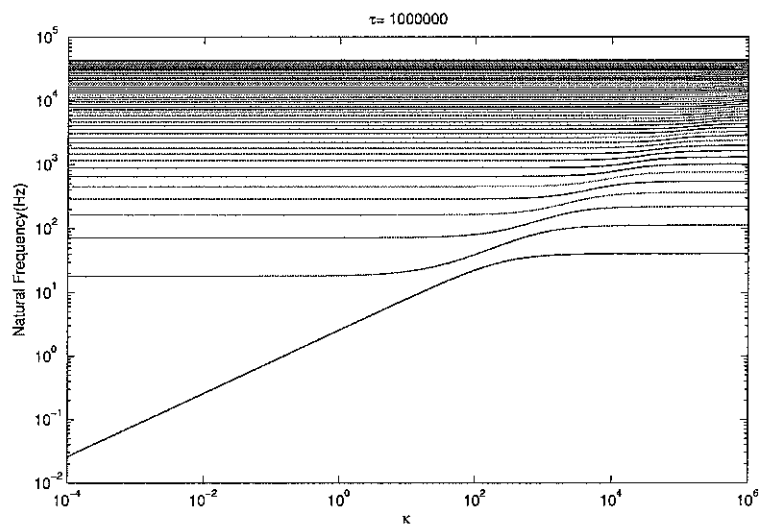
$$\tau = \frac{k_R L}{EI} \quad (3.27)$$

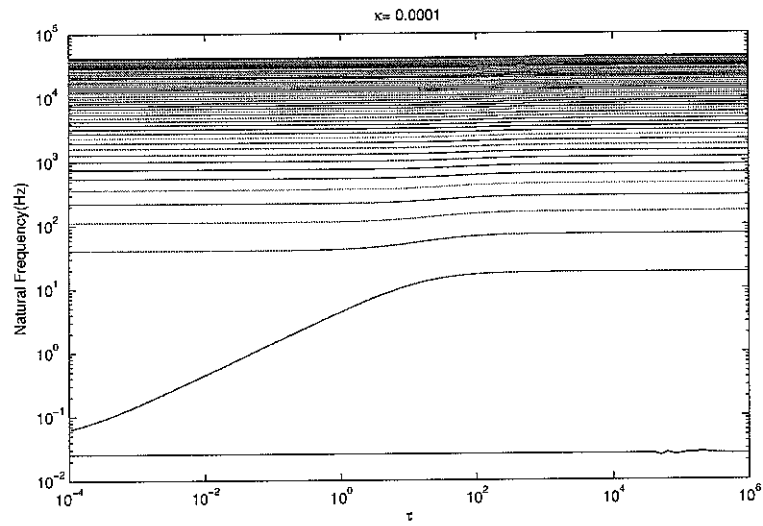
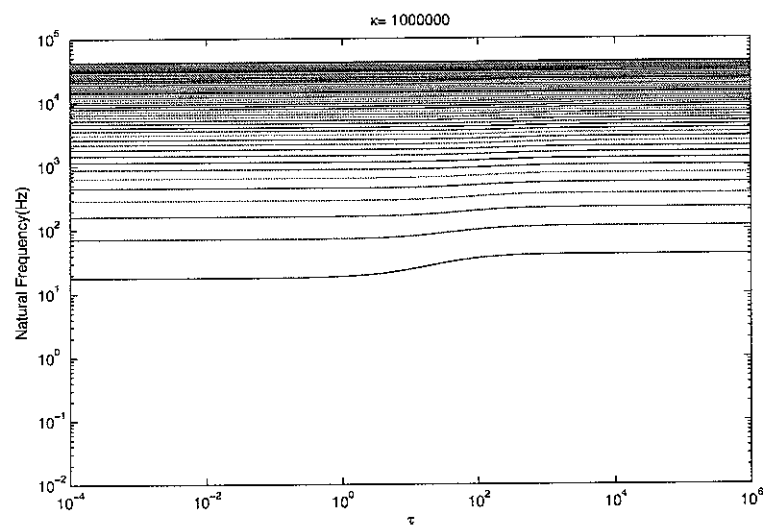
Figure 3.2 shows the variation of the natural frequencies with the linear spring constant when $\tau = 0.0001$ and $\tau = 10^6$. When $\tau = 0.0001$, the beam's dynamics is changed from being free-free to being simply supported as the linear spring constant increases. Figure 3.3 shows the variation of the natural frequencies with the torsional spring constant when $\kappa = 0.0001$ and $\kappa = 10^6$. When $\kappa = 10^6$, the beam's dynamics is changed from being simply supported to being clamped as the torsional spring constant increases. Figures 3.4 to 3.6 show the variation of the natural modes respectively with reference to the linear and rotational stiffness. It can be seen that the first two modes, originally rigid body modes, turn into the flexible modes of a simply supported beam when

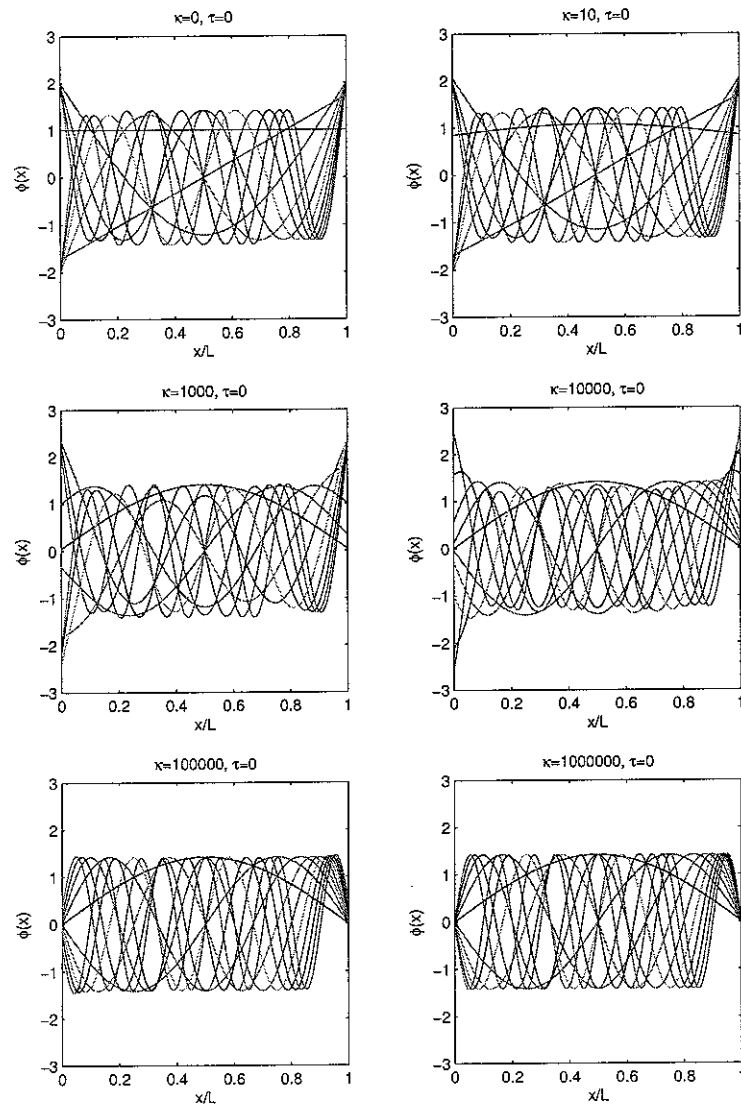
Table 3.1: Mechanical properties and masses

| symbol | value | unit | descriptions |
|--------|-------|------------------------|-----------------|
| E | 65 | MPa | Young's Modulus |
| ρ | 2650 | kg/m^3 | density |
| ν | 0.3 | | Poisson ratio |
| L | 0.50 | m | length |
| b | 0.03 | m | width |
| h | 0.002 | m | thickness |
| η | 0.01 | | loss factor |

$\kappa = 100$. Other higher modes are affected by the mount stiffness at higher values of the stiffness.

(a) when $\tau = 0.0001$ (b) when $\tau = 10^6$ Figure 3.2: Variation of natural frequencies with the linear spring constant, κ

(a) when $\kappa = 0.0001$ (b) when $\kappa = 10^6$ Figure 3.3: Variation of natural frequencies with the rotational spring constant, τ

Figure 3.4: Variation of mode shape with the linear spring constant when $\tau = 0$

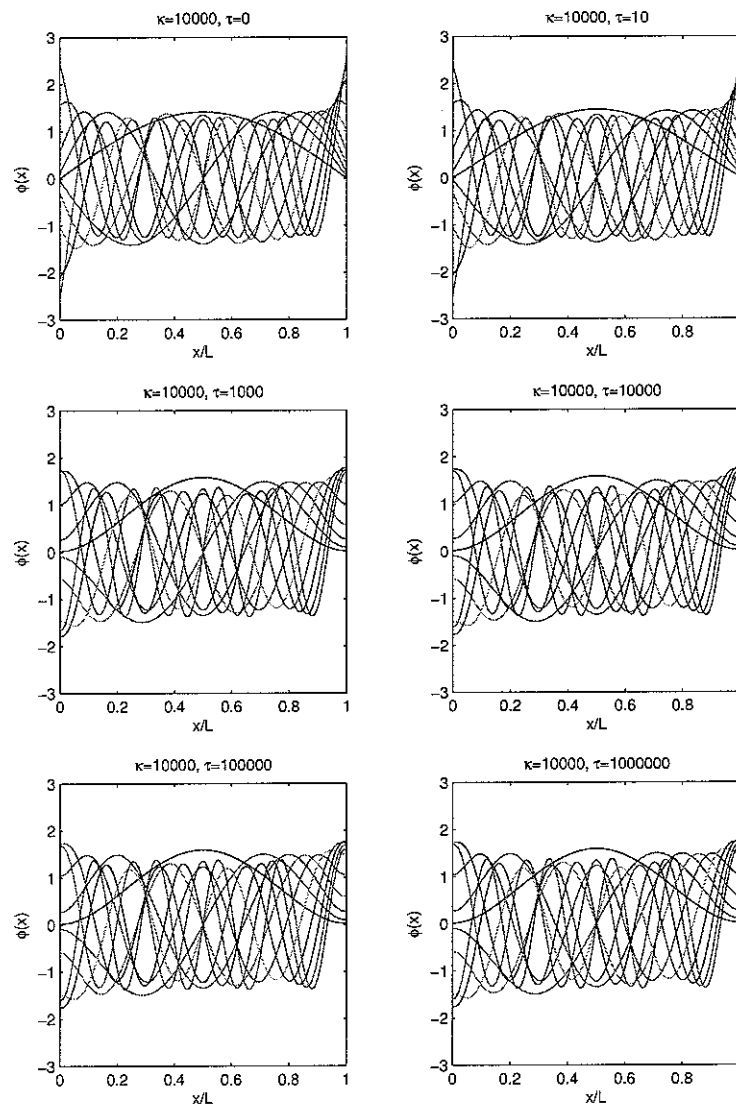


Figure 3.5: Variation of mode shape with the rotational spring constant when $\kappa = 10^4$

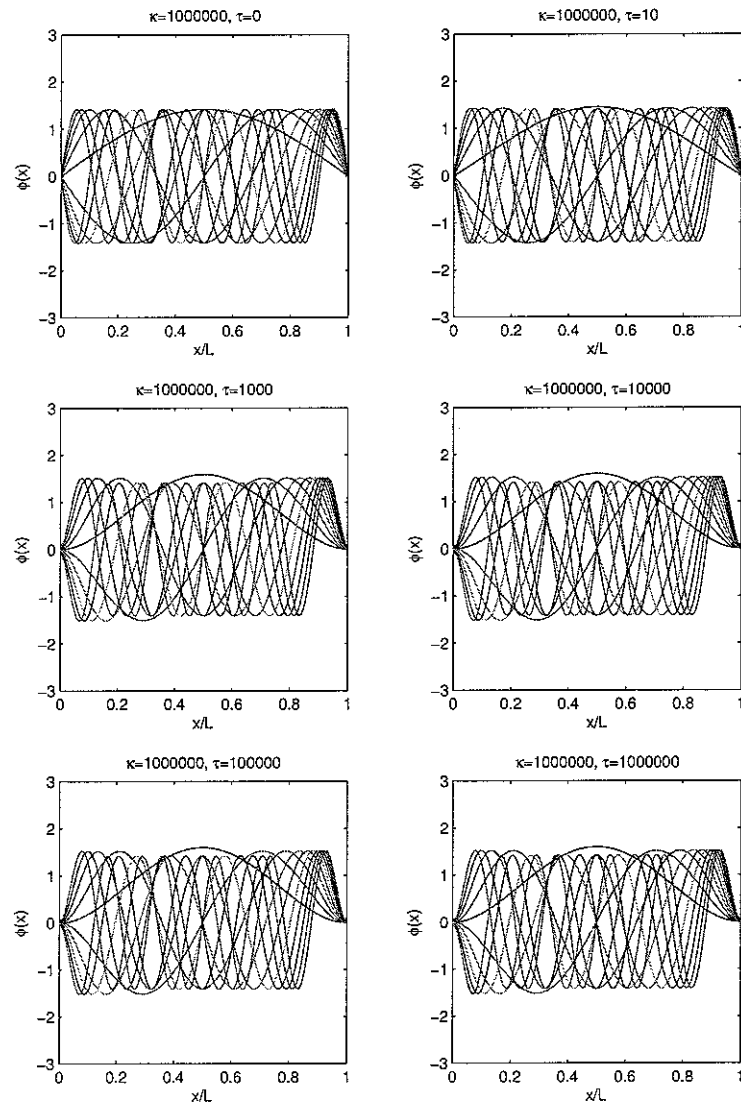


Figure 3.6: Variation of mode shape with the rotational spring constant when $\kappa = 10^6$

3.3 Equivalent Actuation Resultant for Beams

Many researchers[13–15] have used a triangularly-shaped actuator to approximate a linear shading of a piezoelectric actuator in one dimension which gives two concentrated force at both ends and a concentrated moment as shown in Figure 3.7. In the previous applications[13–15], however, a very long triangular actuator covering the whole length of the beam has been used such that the actuator angle was very small, e.g. $\theta_{PZT} < 4.3^\circ$ in reference[15]. In this case the contribution of the moment distribution along the lateral sides can be negligible. Since the shape of the actuator in this study is not constrained, the equivalent actuation for beams due to the triangularly-shaped actuator should be obtained from the two dimensional formulation shown in Figure 2.4 by projecting all component of actuation on the beam axes, x , shown in Figure 3.8. The forces at the vertices of the base edge of the actuator are summed up and act at the left end of the beam. The moments along the base edge is also modelled as a concentrated moment at the left end of the beam. The moments along the lateral sides generate bending and torsional excitation. The bending components along each lateral side are summed, while the torsion components are eliminated when projecting on the beam axes. The resultant one-dimensional equivalent excitation is depicted in Figure 3.9. Note that the expressions in Figures 2.4 and 3.8 are the resultant of the Laplacian operator, thus the moments and forces generated are calculated multiplying $\frac{h_s}{2}v_{cs}(t)$. Therefore, the forced equation of motion of motion for flexible vibrations of a beam with a triangularly-shaped actuator at one end can be expressed as

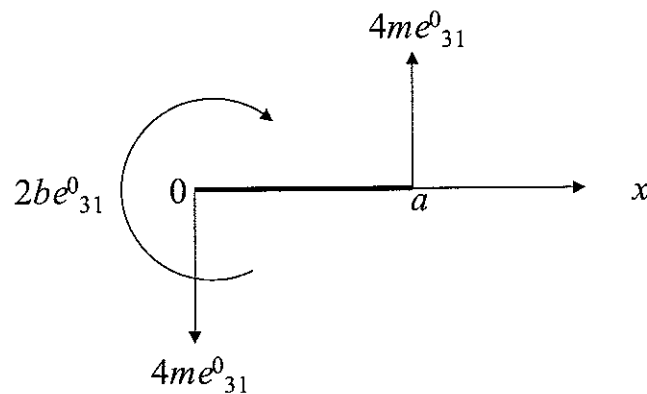


Figure 3.7: Result of Laplacian of one dimensional transducer distribution

$$\begin{aligned}
\mathcal{L}_b(w; x, t) = & \frac{h_s v_{cs}(t)}{2} [4m e_{31}^0 \{\delta(x-a) - \delta(x)\}] \\
& + \frac{h_s v_{cs}(t)}{2} \left[2b e_{31}^0 \frac{\partial \delta(x)}{\partial x} \right] \\
& - \frac{h_s v_{cs}(t)}{2} \left[2(m^2 e_{31}^0 + e_{32}^0) \frac{\sin \theta_{PZT}}{\cos \theta_{PZT}} \frac{\partial}{\partial x} \{U(x) - U(x-a)\} \right]
\end{aligned} \tag{3.28}$$

where $\mathcal{L}_b(w)$ is the beam dynamic operator, shown in Equation 3.2 and $U()$ is the step function. The first term in Equation 3.28 denotes the concentrated forces at $x = 0$ and $x = a$, the second term the concentrated moment at $x = 0$, and third term the distributed moments between $x = 0$ and $x = a$. Since the derivative of the step function with respect to x is the delta function, i.e,

$$\frac{\partial U(x-a)}{\partial x} = \delta(x-a) \tag{3.29}$$

the equation of motion becomes

$$\begin{aligned}
\mathcal{L}_b(w; x, t) = & \frac{h_s v_{cs}(t)}{2} [4m e_{31}^0 \{\delta(x-a) - \delta(x)\}] \\
& + \frac{h_s v_{cs}(t)}{2} \left[2b e_{31}^0 \frac{\partial \delta(x)}{\partial x} \right] \\
& - \frac{h_s v_{cs}(t)}{2} [2m(m^2 e_{31}^0 + e_{32}^0) \{\delta(x) - \delta(x-a)\}]
\end{aligned} \tag{3.30}$$

The third term is now two concentrated forces at $x = 0$ and $x = a$ as shown in Figure 3.10(a). Physically, the distributed moments can be interpreted with pairs of forces generating the moments. However, apart from the forces at the boundary, the internal force components are eliminated each other because of same magnitude with opposite direction by the constant distribution of moment. Figure 3.10(b) shows the equivalent actuation resultant for beams due to the triangular actuator in terms of one concentrated moment at $x = 0$ and two concentrated forces at $x = 0$ and $x = a$, assuming that $d_{3'1'} = d_{3'2'}$ and $d_{3'6'} = 0$ as shown in Table 2.1. The equivalent actuation in Equation 3.30, therefore, becomes

$$\mathcal{L}_b(w; x, t) = m e_{31}^0 h_s v_{cs}(t) \left[(m^2 + 3) \{\delta(x-a) - \delta(x)\} + a \frac{\partial \delta(x)}{\partial x} \right] \tag{3.31}$$

for which the relationship, $b = a \tan \theta_{PZT} = ma$, is used.

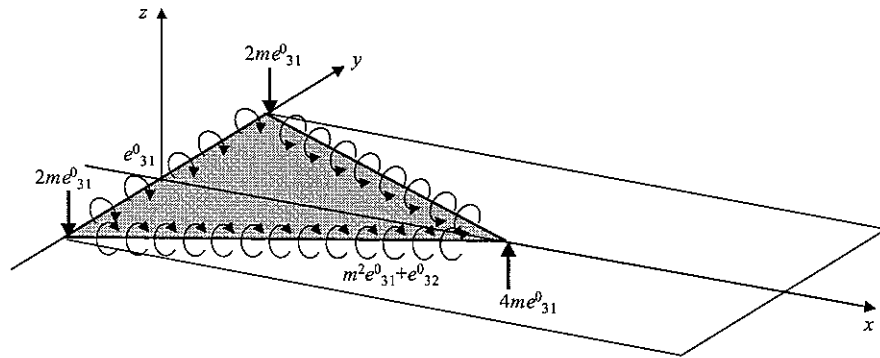


Figure 3.8: Actuation for beams due to the triangularly-shaped actuator obtained from two dimensional approach. Note that the expressions in the figure are the resultant of the Laplacian operator so that the moments and forces generated are calculated multiplying $h_s v_{cs}(t)/2$.

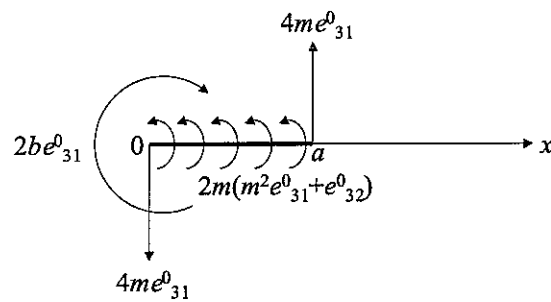
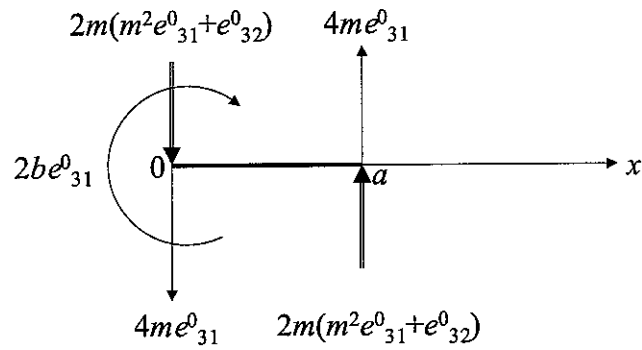
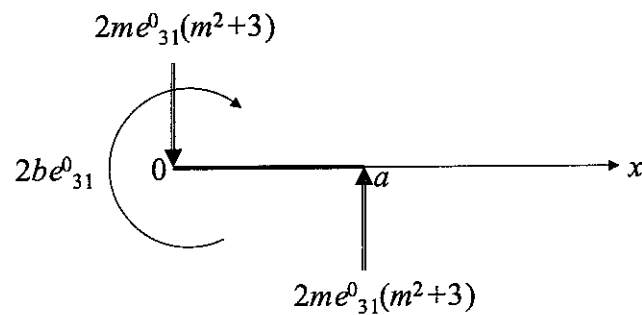


Figure 3.9: Equivalent actuation resultant for beams having a distributed moment term



(a) Equivalent concentrated force of the distributed moments along the sloped side



(b) Equivalent resultant with the assumption of $e_{31}^0 = e_{32}^0$

Figure 3.10: Equivalent actuation resultant for beams with concentrated actuation. Note that the expressions in the figure are the resultant of the Laplacian operator so that the moments and forces generated are calculated multiplying $h_s v_{cs}(t)/2$.

3.4 Beam Response to Triangular Actuator Excitation

The response of beams due to the excitation generated by a triangularly-shaped piezoelectric actuator can be obtained using a modal expansion of the response as highlighted by Equations from A.1 to A.6. Thus the response is modelled as a summation of the modal amplitudes at the response position each multiplied by the corresponding modal excitation generated by triangularly-shaped actuator. The modal excitation can be expressed substituting the right hand side of Equation 3.31 into Equation A.6 as

$$F_n(\omega) = me_{31}^0 h_s V_{cs}(\omega) [(m^2 + 3) \{\phi_n(a) - \phi_n(0)\} - a\phi_n'(0)], \quad (3.32)$$

where $F_n(\omega)$ is modal excitation and $V_{cs}(\omega)$ is the amplitude of the driving voltage. The velocity response per unit driving voltage, which is referred as to the *transfer function*, can then be expressed as

$$Y(x, \omega) = \sum_{n=1}^{\infty} \frac{j\omega\phi_n(x)me_{31}^0 h_s}{\rho AL[(1 + j\eta)\omega_n^2 - \omega^2]} [(m^2 + 3) \{\phi_n(a) - \phi_n(0)\} - a\phi_n'(0)]. \quad (3.33)$$

It is useful for physical interpretations to divide this expression into four functions for each term of actuation, a point force at $x = 0$, another point force at $x = a$, a point moment at $x = 0$ and a distributed moment at $0 \leq x \leq a$.

For the point force at $x = 0$,

$$Y_{f0}(x, \omega) = \sum_{n=1}^{\infty} \frac{j\omega\phi_n(x)me_{31}^0 h_s}{\rho AL[(1 + j\eta)\omega_n^2 - \omega^2]} [-2\phi_n(0)], \quad (3.34)$$

for the point force at $x = a$,

$$Y_{fa}(x, \omega) = \sum_{n=1}^{\infty} \frac{j\omega\phi_n(x)me_{31}^0 h_s}{\rho AL[(1 + j\eta)\omega_n^2 - \omega^2]} [2\phi_n(a)], \quad (3.35)$$

for the point moment at $x = 0$,

$$Y_{m0}(x, \omega) = \sum_{n=1}^{\infty} \frac{j\omega\phi_n(x)me_{31}^0 h_s}{\rho AL[(1 + j\eta)\omega_n^2 - \omega^2]} [-a\phi_n'(0)], \quad (3.36)$$

and finally for the distributed moment at $0 \leq x \leq a$,

$$Y_{md}(x, \omega) = \sum_{n=1}^{\infty} \frac{j\omega\phi_n(x)me_{31}^0 h_s}{\rho AL[(1 + j\eta)\omega_n^2 - \omega^2]} [\sec \theta_{PZT} \{\phi_n(a) - \phi_n(0)\}]. \quad (3.37)$$

Chapter 4

Direct Velocity Feedback Control for Beams using a Triangular Actuator

4.1 Formulation

Figure 4.1 shows the schematic arrangement and the block diagram of the feedback control system for the beam. The feedback gain will be assumed to be constant so that direct velocity feedback control is implemented. The total velocity response at x_r can be expressed as

$$v_r(x_r, \omega) = Y_{pr}(j\omega)f_p + Y_{sr}(j\omega)V_{cs} \quad (4.1)$$

where Y_{pr} is the mobility function due to the primary force, f_p at x_p given by

$$Y_{pr}(j\omega) = \sum_{n=1}^N A_n(j\omega)\phi_n(x_p)\phi_n(x_r) \quad (4.2)$$

and Y_{sr} is the transfer function defined in Equation 3.33 at $x = x_r$, given by

$$Y_{sr}(j\omega) = \sum_{n=1}^{\infty} A_n(j\omega)\phi_n(x_r)m e_{31}^0 h_s [(m^2 + 3) \{\phi_n(a) - \phi_n(0)\} - a\phi_n'(0)]. \quad (4.3)$$

$A_n(j\omega)$ is given by Equation A.5.

Therefore, the sensor output before control, d , and the transfer function of the plant

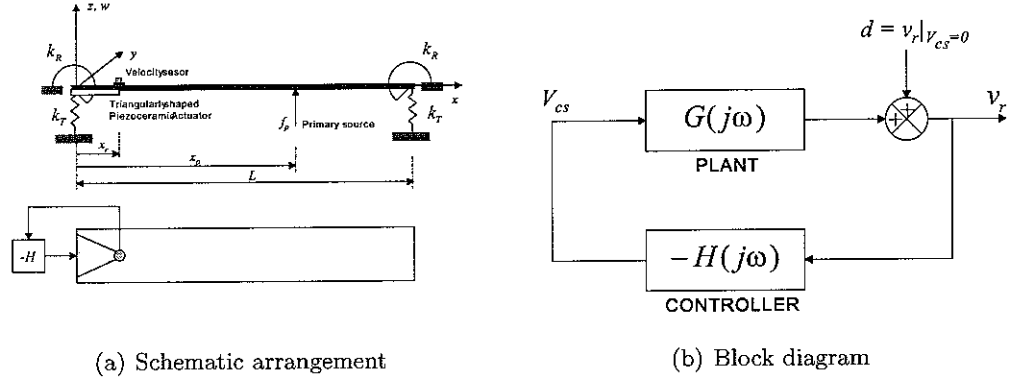


Figure 4.1: Active feedback control system using a triangular-shaped piezoceramic actuator

are given by $d(j\omega) = Y_{pr}(j\omega)f_p$ and $G(j\omega) = Y_{sr}(j\omega)$, respectively. So, Equation 4.1 can be written as

$$v_r(j\omega) = d(j\omega) + G(j\omega)V_{cs}. \quad (4.4)$$

The driving voltage fed back from the velocity sensor, V_{cs} , is represented by the sensor output multiplied by the feedback gain, i.e.,

$$V_{cs}(j\omega) = -v_r(j\omega)H(j\omega) \quad (4.5)$$

Provided the control system is stable, the spectrum of the total velocity output, v_r , is related to the spectrum of the sensor output before control, d , as follow.

$$\frac{v_r(j\omega)}{d(j\omega)} = \frac{1}{1 + G(j\omega)H(j\omega)}. \quad (4.6)$$

The Nyquist stability criterion is used as a graphical method for determining the stability of a closed-loop system by investigating the properties of the frequency-domain plots of $G(j\omega)H(j\omega)$. For the closed-loop control system expressed by Equation 4.6 to be stable, the Nyquist plot of $G(j\omega)H(j\omega)$ must encircle the $(-1, j0)$ point as many times as the number of poles of $G(j\omega)H(j\omega)$ that are in the right half of the s -plane, and the encirclement, if any, must be made in the clockwise direction [16]. In this case, both G and H are stable, so instability is indicated by any enclosure. The total response to the primary disturbances and the secondary control action can be obtained. Also, from Equation 4.5, the secondary control action can be expressed as

$$V_{cs} = \frac{-H(j\omega)Y_{pr}(j\omega)}{1 + G(j\omega)H(j\omega)}f_p \quad (4.7)$$

Assuming the feedback gain to be constant, and employing the relationship, $G(j\omega) =$

$Y_{sr}(j\omega)$, to the Equation 4.7, the secondary control action is rewritten as

$$V_{cs} = \frac{-hY_{pr}(j\omega)}{1 + hY_{sr}(j\omega)} f_p \quad (4.8)$$

The response of the beam with the control system can be derived in terms of the product of the vector with the modal amplitudes at the response position and the vector with the modal velocity excitations as given by Equation A.7. The modal amplitude vector in Equation A.7 relative to the total response can be defined as

$$\mathbf{a} = \mathbf{a}_p + \mathbf{a}_{cs}, \quad (4.9)$$

where \mathbf{a}_p is the vector with the modal amplitudes due to the primary force, f_p , given by

$$\mathbf{a}_p = f_p \{A_1\phi_1(x_p), A_2\phi_2(x_p), \dots, A_n\phi_n(x_p)\}^T, \quad (4.10)$$

and \mathbf{a}_{cs} is the vector with the modal amplitude due to the control action by the triangularly-shaped piezoceramic actuation with V_{cs} , given by

$$\mathbf{a}_{cs} = \{A_1F_1, A_2F_2, \dots, A_nF_n\}^T. \quad (4.11)$$

Substituting Equation 4.8 into the Equation 3.32 yields the modal force, F_n , due to the actuation. The kinetic energy and the acoustic power can now be estimated by Equations A.11 and A.12, respectively, to evaluate the control performance.

4.2 Plant Response and Stability

4.2.1 Effect of the Boundary Condition

The plant response, $Y_{sr}(j\omega)$, is the velocity response at $x = x_r$ generated by the triangularly-shaped actuator with the unit driving voltage, i.e $V_{cs} = 1$, which can be evaluated by Equation 3.33. It can be written in the form;

$$Y_{sr}(x_r, \omega) = \sum_{n=1}^{\infty} A_n(j\omega) m e_{31}^0 h_s \phi_n(x_r) [(m^2 + 3) \{\phi_n(a) - \phi_n(0)\} - a\phi_n'(0)]. \quad (4.12)$$

The behaviour of the plant response thus depends on the boundary conditions (κ and τ), the shape dimensions of the triangular (a , b , or θ_{PZT}) and the location of the sensor (x_r).

For the initial simulations, the beam is assumed to be clamped at both ends ($\kappa = \infty$

and $\tau = \infty$) and the sensor is located at $x = a$. The actuator's dimensions defined in Figure 2.3 are assumed to be $a = 25\text{mm}$ and $b = 15\text{mm}$, i.e., $\theta_{PZT} = 31^\circ$. Since $\phi_n(0) = 0$ and $\phi'_n(0) = 0$, when the beam is clamped at both ends, the plant response of the clamped beam can be written as

$$G(j\omega) = Y_{sr}^{(cc)}(a, \omega) = \sum_{n=1}^{\infty} A_n(j\omega) m e_{31}^0 h_s (m^2 + 3) \phi_n^2(a). \quad (4.13)$$

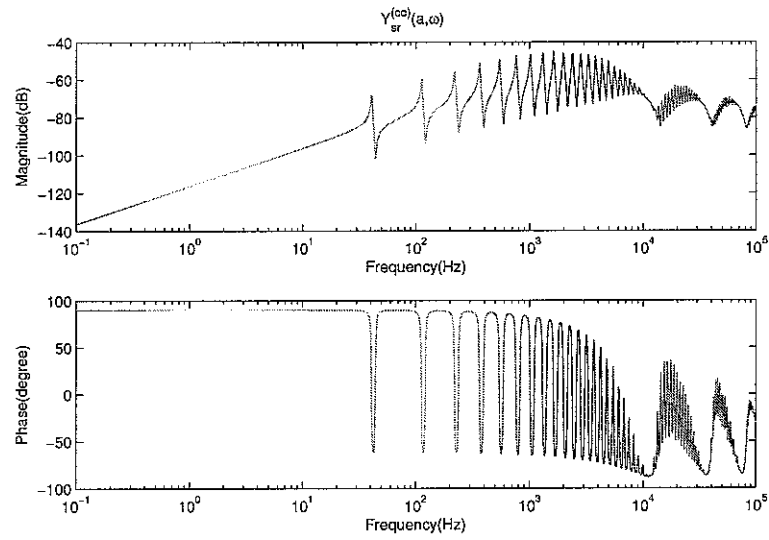
Since $\sec\theta_{PZT} > 0$ and $m = \tan\theta_{PZT} > 0$ for the physically possible shapes, i.e., $\theta_{PZT} > 90^\circ$, it can be expected that the phase of the plant response always stays between $\pm 90^\circ$, and so the control system is to be *unconditionally stable*¹. Figure 4.2 shows the velocity sensor-triangular actuator plant response of a clamped beam with the sensor at $x = a$. The phase is confined between $\pm 90^\circ$ and the Nyquist curve stays in the right hand side, showing the unconditional stability. Dips in the response function at about 10kHz, 40kHz and 80kHz are due to the sensor position located at a node. Those frequencies are corresponding to the n -th natural frequencies such that the first, second or third nodal point of the n -th mode is equal to the height of actuator, a . As discussed in Chapter 3 those frequencies decrease as the stiffness of the boundary, κ and/or τ decrease since the corresponding nodal points occurs at lower modes. The frequency of these drops can be obtained explicitly for a simply supported beam since the coordinate of the first nodal point of the n -th mode can be expressed as L/n for $n > 2$.

When the beam is simply-supported ($\kappa = \infty$ and $\tau = 0$), $\phi_n(0) = 0$ but $\phi'_n(0) \neq 0$. The plant response can be expressed as

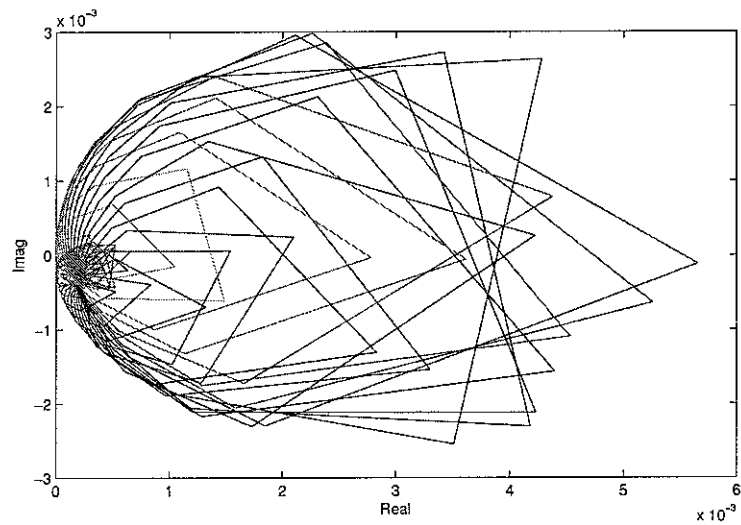
$$G(j\omega) = Y_{sr}^{(ss)}(a, \omega) = \sum_{n=1}^{\infty} A_n(j\omega) m e_{31}^0 h_s \phi_n(a) [(m^2 + 3)\phi_n(a) - a\phi'_n(0)]. \quad (4.14)$$

Thus the moment at $x = 0$ couples into the modes while the force at $x = 0$ does not. Since the moment couples more efficiently into higher modes, an extra phase shift occurs at a high frequency. Figure 4.3 shows the the velocity sensor-triangular actuator plant response for a simply-supported beam when the sensor is located at $x = a$. It can be seen that the control system is only conditionally stable with gain margin of about 65dB. The conditional stability is due to the existence of the non-collocated, non-dual moment actuation at $x = 0$. The response at the sensor location is given by the sum of the response due to the concentrated force at $x = a$ shown in Figure 4.4(a) and the response due to the distributed moment between $x = 0$ and $x = a$ shown in Figure 4.4(a). At frequencies below 7kHz, the two responses are out-of-phase but

¹However, it should be noted that the distributed moments along the inclined edge of the actuator can couple into the transverse plate modes so that unconditional stability is not anymore guaranteed.



(a) Bode diagram



(b) Nyquist plot

Figure 4.2: Plant response for a clamped beam from the triangularly-shaped piezoceramic actuator to the velocity sensor at $x = a$.

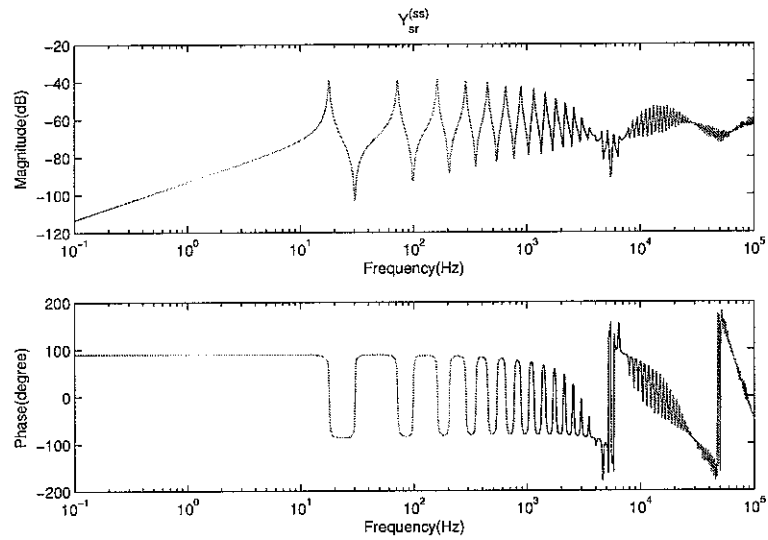
the magnitude due to the forces is much bigger than the other. The phase of the total response shown in Figure 4.3 stays between $\pm 90^\circ$. Around 7kHz, however, the response due to the force goes down because the corresponding normal modes have their nodes around sensor location leading to a small response but also inefficient actuation. Since the moment excitation component is located at the end of the beam away from the sensor and couples efficiently into higher order modes, the response due to the moment excitation component remains relatively large at higher frequencies. However, the total response at higher frequencies where the phase exceeds -90° is still small compared to the low frequency where the phase is between $\pm 90^\circ$ so that a large gain margin is available. This phase characteristics can be seen from the modal coupling factor given by

$$\Gamma_n = \phi_n(a) [(m^2 + 3)\phi_n(a) - a\phi_n'(0)], \quad (4.15)$$

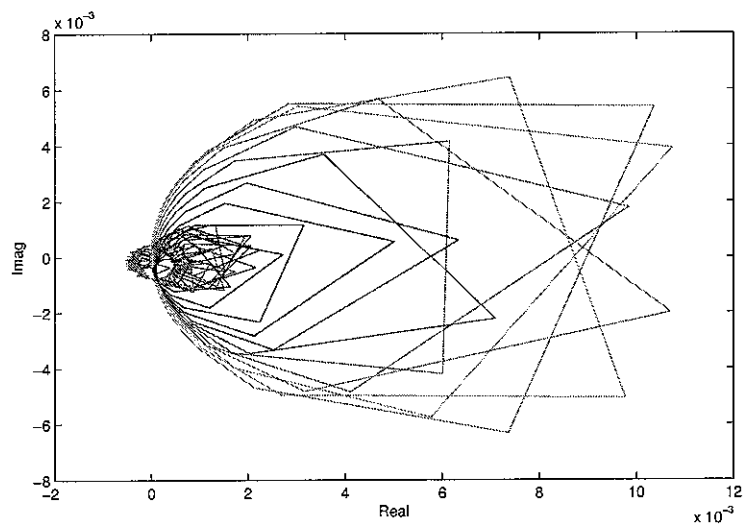
where Γ_n is the modal coupling factor. Since the phase of $A_n(j\omega)$ in Equation 4.14 always stays between $\pm 90^\circ$, the phase shift occurs when the sign of the modal coupling factor is changed from positive to negative. Figure 4.5 shows the variation of the sign of the modal coupling factor with the mode index, n , and the shape of the piezoceramic actuator, θ_{PZT} . It can be seen that, for this actuator, the phase shift is first introduced by the 15th and the 20th modes whose effect becomes predominant at their resonances, which agrees with the total plant response shown in Figure 4.3(a). Also, it can be seen from Figure 4.5 that the phase change effect can not be removed by changing the angle of the actuator, however it can be moved to higher order modes by narrowing the angle.

One possible way to remove the phase shift is to increase the rotational spring constant. Assuming that $\kappa \rightarrow \infty$, the plant response is expressed as in Equation 4.14, but $\phi_n'(0)$ decreases as τ increases as shown in Figure 3.6 so that the sign of the modal coupling factor, shown in Equation 4.15, changes sign at higher n . Figure 4.6 shows the variation with the rotational spring constant at both ends of the open loop velocity sensor-triangular actuator plant response for a simply-supported beam with the rotational springs. It can be seen that the phase shift is moved up from low frequencies to high frequencies as the rotational spring constant increases. It is noted however that the plant response is decreased at low frequencies as the rotational spring constant increases. It is hence necessary to trade off between performance and robustness. Figure 4.7 shows Nyquist plots of the four plant responses which show that the gain margin is increased as the rotational spring constant increases.

To investigate the effect of the translational spring constant, a beam with the boundary condition shown in Figure 4.8 is considered. The angular displacement at the ends is fully constrained while the translation is only partly constrained by the linear springs. For this case, $\phi_n'(0) = 0$, and so the plant response can be obtained from Equation 4.12



(a) Bode diagram



(b) Nyquist plot

Figure 4.3: Plant response for a simply-supported beam from the triangularly-shaped piezoceramic actuator to the velocity sensor at $x = a$.

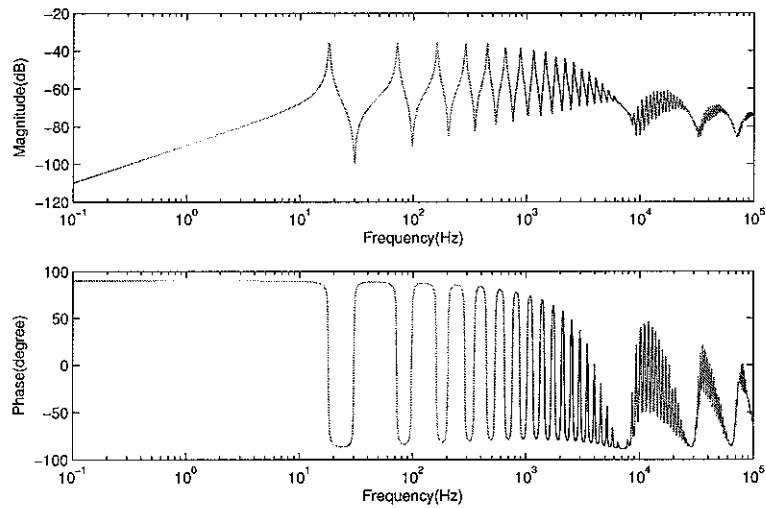
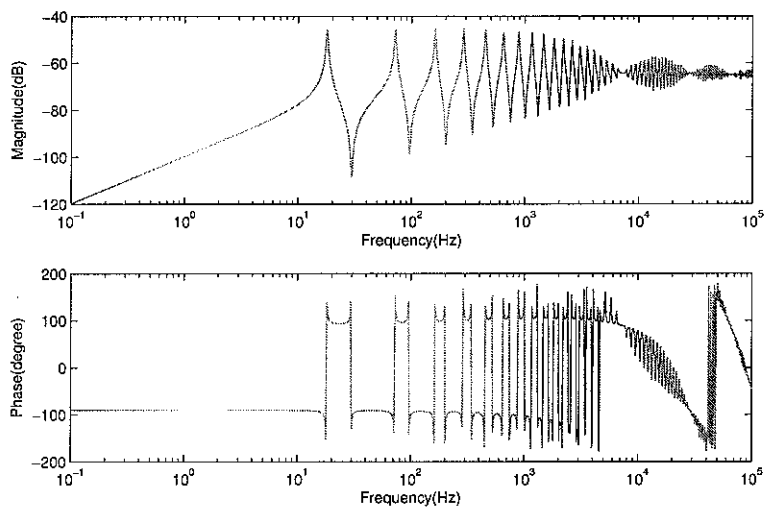
(a) due to collocated forces at $x = a$ (b) due to moment at $x = 0$

Figure 4.4: Components of the plant response for a simply-supported beam from the triangularly-shaped piezoceramic actuator to the velocity sensor at $x = a$; (a) due to collocated forces at $x = a$ and (b) due to moment $x = 0$.

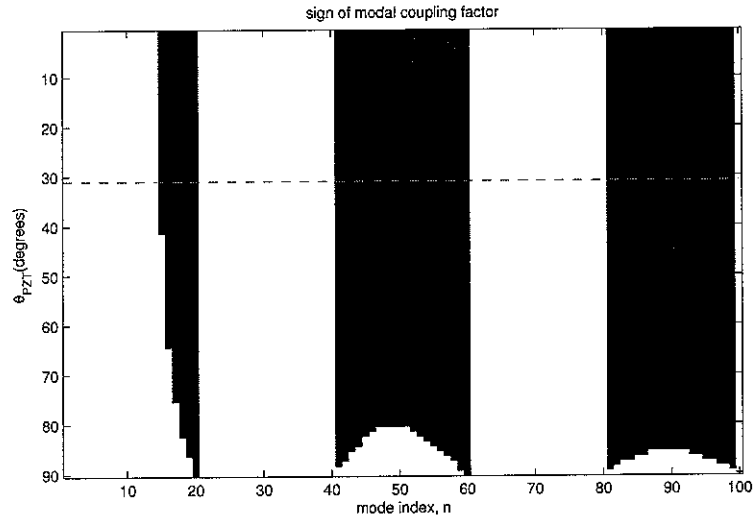


Figure 4.5: Variation of the sign of the modal coupling factor with the mode index, n , and the shape of the piezoceramic actuator, θ_{PZT} . The white region denotes stable modes and the black region unstable.

as

$$Y_{sr}(x_r, \omega) = \sum_{n=1}^{\infty} A_n(j\omega) m e_{31}^0 h_s \phi_n(x_r) [(m^2 + 3) \{\phi_n(a) - \phi_n(0)\}]. \quad (4.16)$$

Figure 4.9 shows the velocity sensor-triangular actuator plant response for beams with the boundary condition $\tau = \infty$ and $\kappa = 0$. It displays a marked instability effect as shown in Figure 4.9(b). When $\kappa \rightarrow 0$, $\phi_n(a) \approx \phi_n(0)$ (assuming $\phi_n(a) > 0$) at frequencies less than n -th natural frequency ($f < f_n$) such that $n \approx L/a$. Therefore $Y_{sr}(x_r, \omega) \rightarrow 0$, as can be seen in Equation 4.16, where f_n is about 2kHz in this case. Precisely, at such frequencies, $\phi_n(a) < \phi_n(0)$ and thus the phase of the plant response is outside the range of $\pm 90^\circ$. Figure 4.10 shows the contribution of each actuation component of the triangularly-shaped piezoactuator. It can be seen that the contribution due to the forces at $x = 0$ and $x = a$ are almost of the same magnitude but the response due to the force at $x = 0$ is slightly bigger and with opposite phase at low frequencies. The total plant response is hence characterised by a phase outside the $\pm 90^\circ$ range. As can be seen from Figures 3.5 and 3.6, the contribution of the forces at $x = 0$ to the response at the sensor location can be reduced by increasing the linear spring constant since $\phi_n(0)$ is decreased as the linear spring constant is increased.

Figure 4.11 shows the variation of the velocity sensor-triangular actuator open loop frequency response with the linear spring constant (κ) for beams with the boundary condition $\tau = \infty$ at both ends. When imposing linear springs with $\kappa = 1000$ to the beam, shown in Figure 4.8, the phase of the first three modes is in the range $\pm 90^\circ$. When the stiffness is increased to $\kappa = 10^4$, the phase is in the range $\pm 90^\circ$ for the

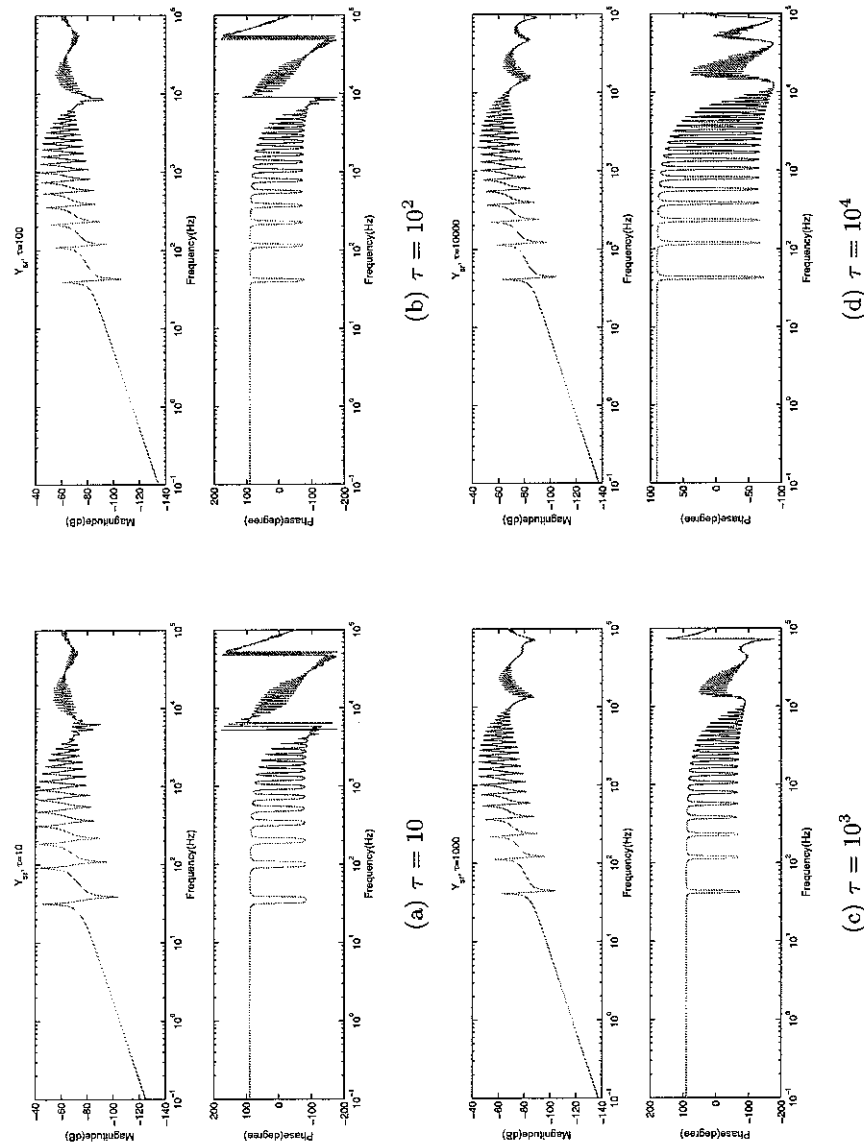


Figure 4.6: Variation with the rotational spring constant at both ends in the bode diagram of the plant response for a simply-supported beam from the triangularly-shaped piezoceramic actuator to the velocity sensor at $x = a$

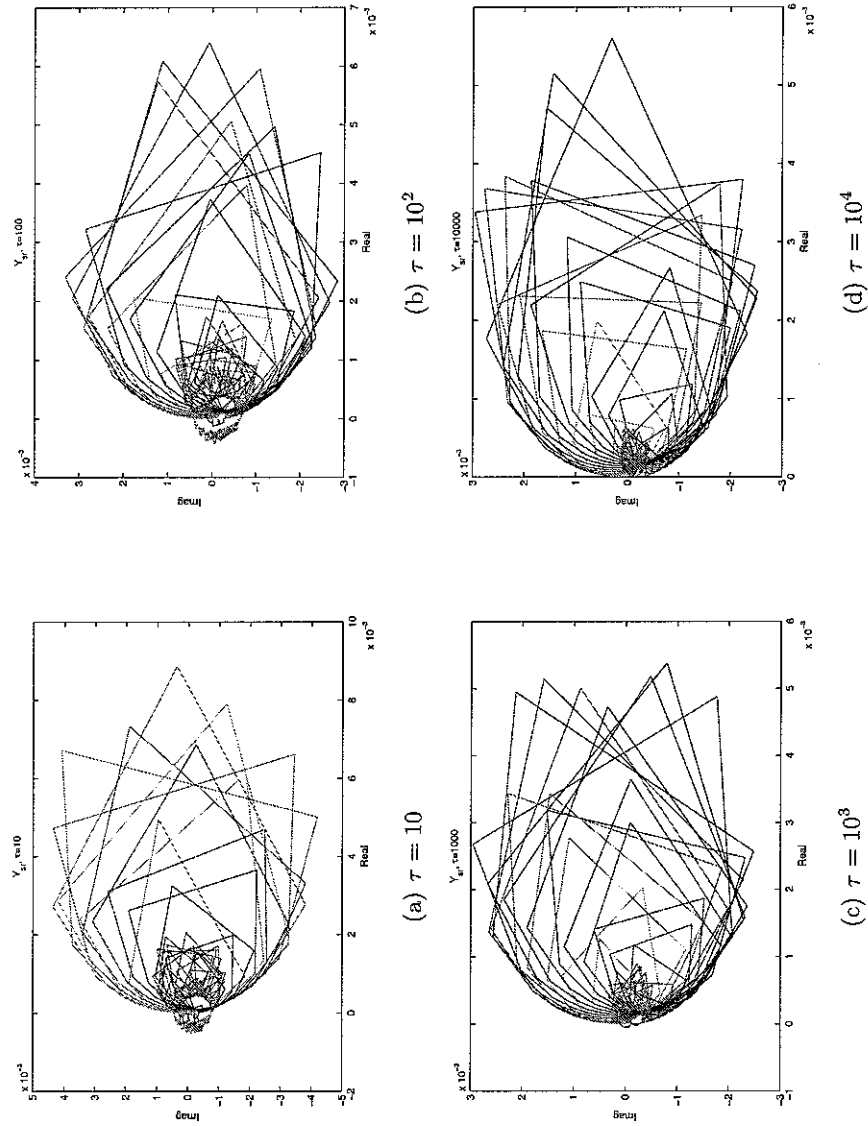


Figure 4.7: Variation with the rotational spring constant at both ends in the Nyquist plot of the plant response for a simply-supported beam from the triangularly-shaped piezoceramic actuator to the velocity sensor at $x = a$

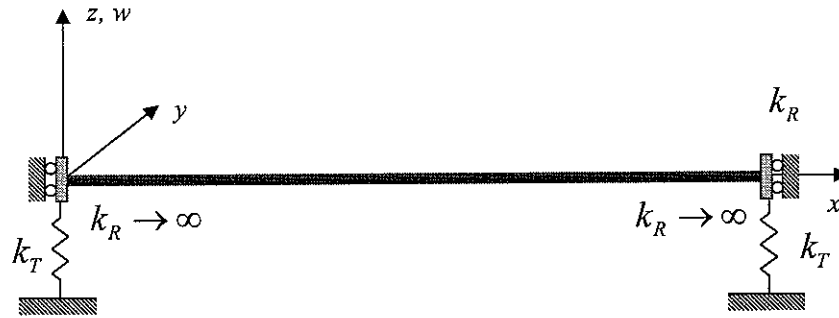
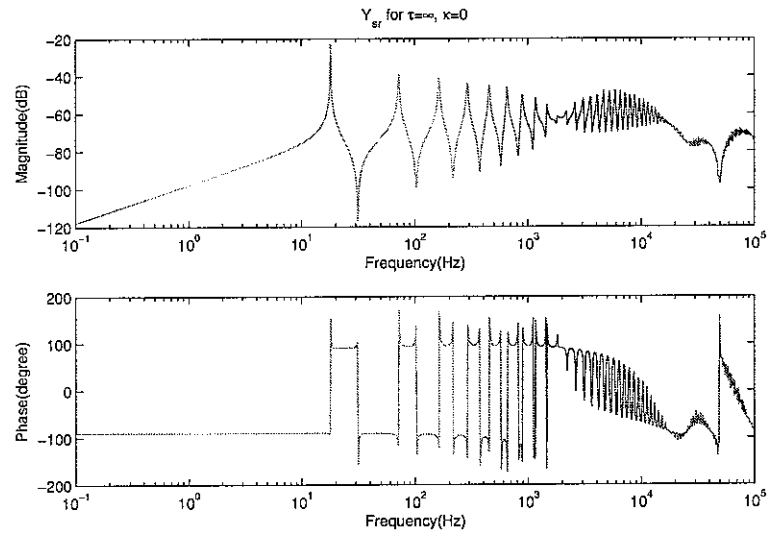


Figure 4.8: Boundary condition to investigate the effect of the linear spring on the stability of the control system.

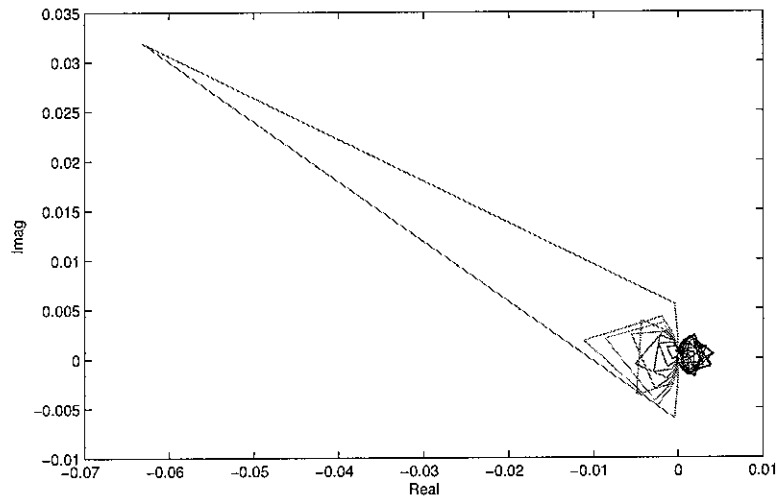
response up to 6th resonating mode, but the response at the first resonating mode is decreased by about 20dB. Increasing the stiffness further to $\kappa = 10^5$, the phase shift is obtained in correspondance to the first dip which is caused by the height of the actuator. Increasing the stiffness further to $\kappa = 10^6$, the plant response is almost the same as that of the clamped beam shown in Figure 4.2 and thus has a large gain margin. Figure 4.12 shows the Nyquist plots of the open loop velocity sensor-triangular actuator as the linear spring constant is varied. It can be seen that the gain margin increases as the linear spring constant increases. It is however noted that the plant response at low frequencies decreases as the linear spring constant increases. Therefore, it is necessary also in this case to trade off between the performance and robustness of the control system.

The effect of the boundary conditions on the stability of the direct velocity feedback control system using the triangularly-shaped piezoceramic actuator has been examined so far. The rotational springs at the two boundaries affects the frequency response only at the dips caused by the height of the actuator. However, the influence is not serious because a high gain margin can be obtained. The linear spring affects seriously the stability at the low frequencies starting from the n -th resonance where the first nodal point of the n -th mode reaches the height of the actuator. A required stiffness can be found for a given beam and actuator. For the case under study, the linear spring constant should be greater than $\kappa = 10^5$ to obtain a high gain margin. Although it is possible to obtain a higher gain margin with a higher linear spring constant and/or a higher rotational spring constant, the control performance depends on the amplitude of the plant response. Since the rotational spring tends to cause the plant response to decrease, there exists an optimal value for the best tradeoff between stability and control performance. To describe this effect, performance index(PI) is defined as

$$PI = GM + PR \quad (\text{dB}), \quad (4.17)$$

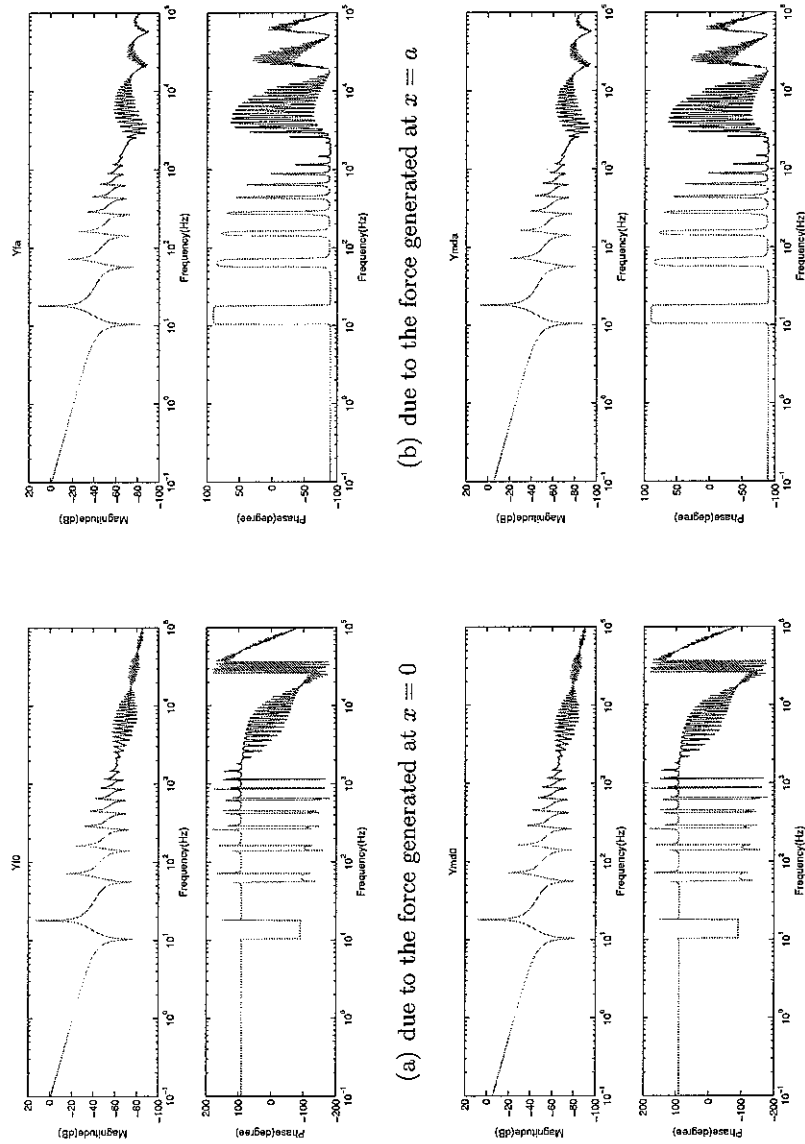


(a) Bode diagram



(b) Nyquist plot

Figure 4.9: Plant response for beams with the boundary condition $\tau = \infty$ and $\kappa = 0$ from the triangularly-shaped piezoceramic actuator to the velocity sensor at $x = a$.



(c) due to the equivalent force positioned at $x = 0$ gen- (d) due to the equivalent force positioned at $x = a$ gen-
 erated by the distributed moment along the actuator erated by the distributed moment along the actuator

Figure 4.10: Components of the plant response for beams with the boundary condition $\tau = \infty$ and $\tau = 0$ from the triangularly-shaped piezoceramic actuator to the velocity sensor at $x = a$

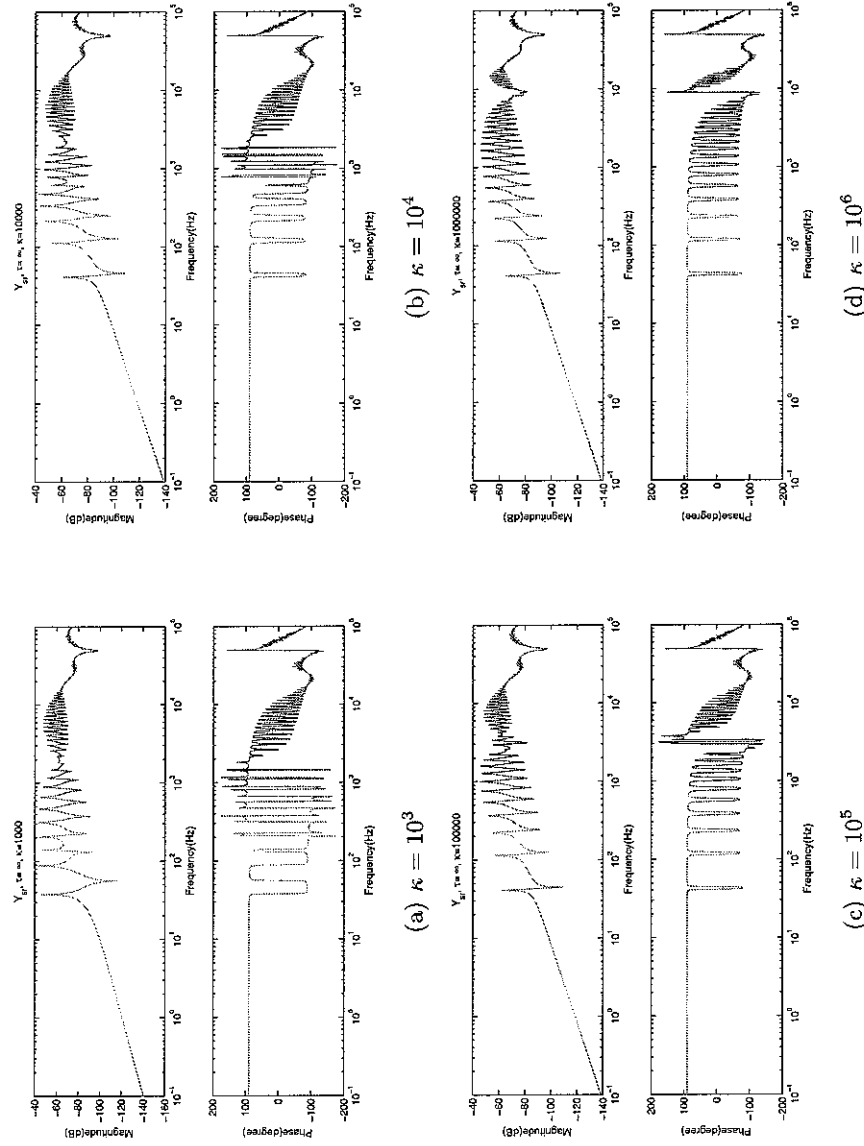


Figure 4.11: Variation with the linear spring constant in the bode diagram of the plant response for beams with the boundary condition $\tau = \infty$ at both ends from the triangular-shaped piezoceramic actuator to the velocity sensor at $x = a$

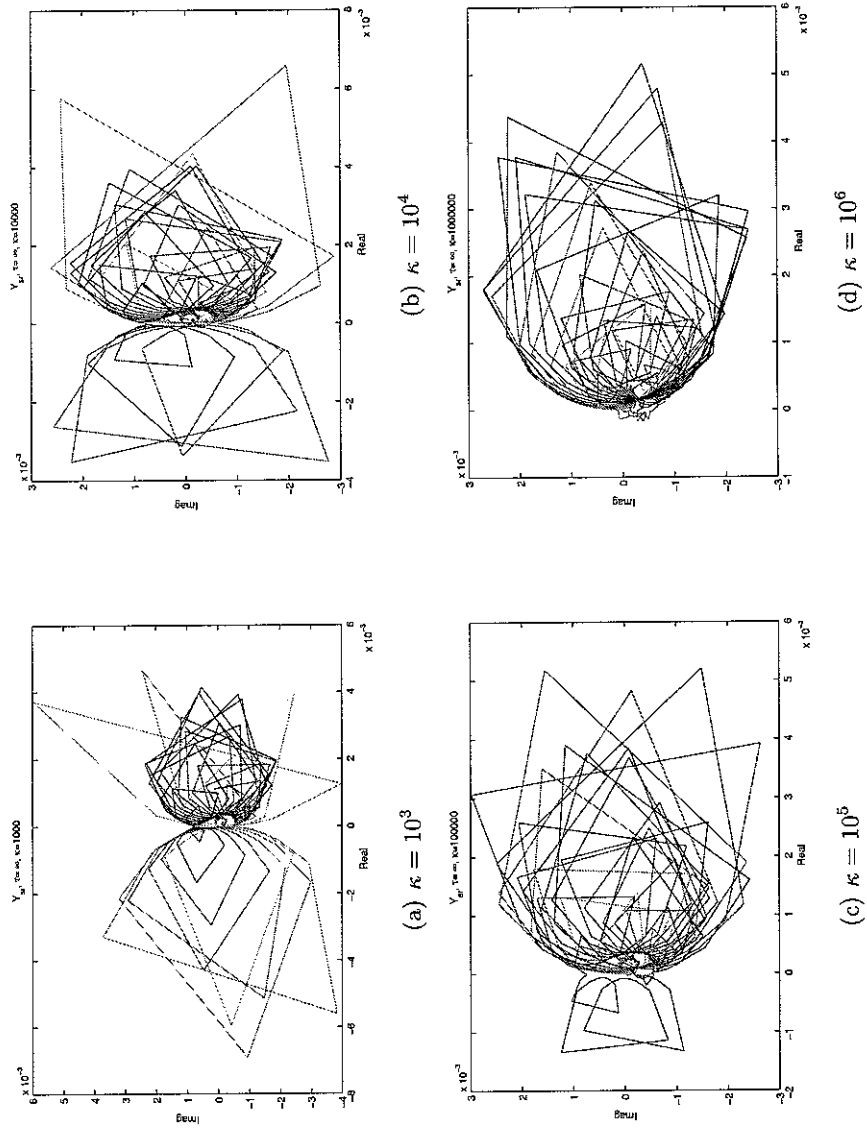


Figure 4.12: Variation with the linear spring constant in the Nyquist plot of the plant response for beams with the boundary condition $\tau = \infty$ at both ends from the triangularly-shaped piezoceramic actuator to the velocity sensor at $x = a$

where GM is the gain margin in dB and PR is the maximum plant response expressed by

$$\text{PR} = 20 \log_{10}(Y_{aa})_{\max} \text{ (dB)}. \quad (4.18)$$

Figure 4.13 shows the variation of those three values in terms of the linear spring constant and the rotational spring constant. It can be seen from Figure 4.13(a) that, at low linear spring constants up to $\kappa = 10^4$, the rotational spring helps to increase the gain margin while at higher linear spring constants the rotational spring does not affect the gain margin. It can be also seen from Figure 4.13(b) that, at low rotational spring constants up to $\kappa = 10^2$, the linear spring decreases the maximum plant response, while at higher rotational spring constants the linear spring does not affect the maximum plant response. It can be found, therefore, as shown Figure 4.13(c) that the performance index is increased as the linear spring constant increases while it is decreased at $\tau = 20$ when $\kappa = 10^6$ as the rotational spring constant increases. Note, however, that the stiffness when $\tau = 20$ does not strongly couple into flexible modes as shown in Figure 3.3(b). This means that the active control system using a triangularly-shaped piezoceramic actuator can yield a reasonable performance for a beam with practical boundary condition with a high linear spring constant.

It is also noted that the control performance is to be limited by the new boundary effect of the actuator at a high feedback gain[17].

4.2.2 Effect of the Actuator Shape

The stability is also affected by the shape of the actuator. The shape of the actuator can be defined by the height of the triangularly-shaped actuator, a , and its half top angle, θ_{PZT} . Since the plant response varies with the location of the velocity sensor, which corresponds to the height of the actuator in this case, the effect of the shape is examined first by keeping the height constant. The width of the beam is assumed as large as the width of the base of the triangular actuator. The ratio of the actuation resultants hence depends only on the angle for given beam and actuator material as shown in Figure 3.10. The actuator shape considered first is shown in Figure 4.14 with the top angles of $\theta_{PZT} = 15^\circ, 30^\circ, 45^\circ, 60^\circ, 75^\circ$. The plant responses are calculated for the five shapes and shown in Figure 4.15. It is found that the magnitude of the plant response increase monotonically as increasing θ_{PZT} having the same phase characteristics up to the frequency where the moment along the base of the actuator begins to affect the total response, which is about 3kHz in this case. In this context it can be also seen that the gain margin decreases while the maximum amplitude of the plant response increases as θ_{PZT} increases, so that the performance index is almost the same, which is

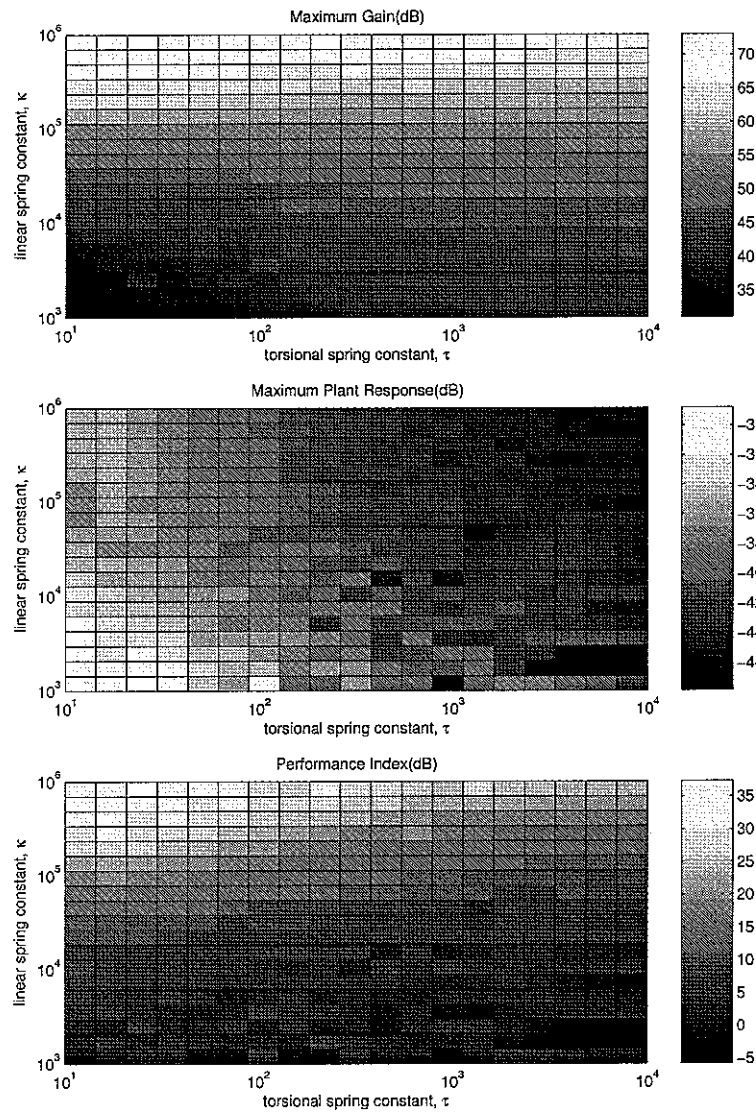


Figure 4.13: Maximum gain, maximum plant response and performance index with respect to the spring constants

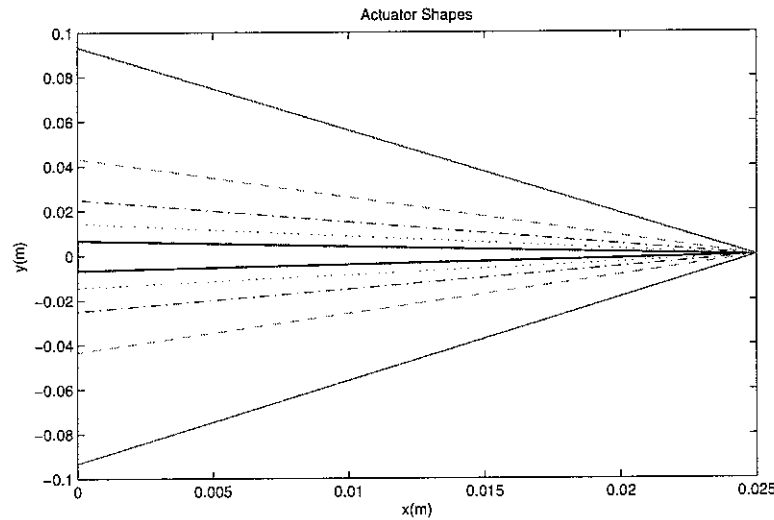
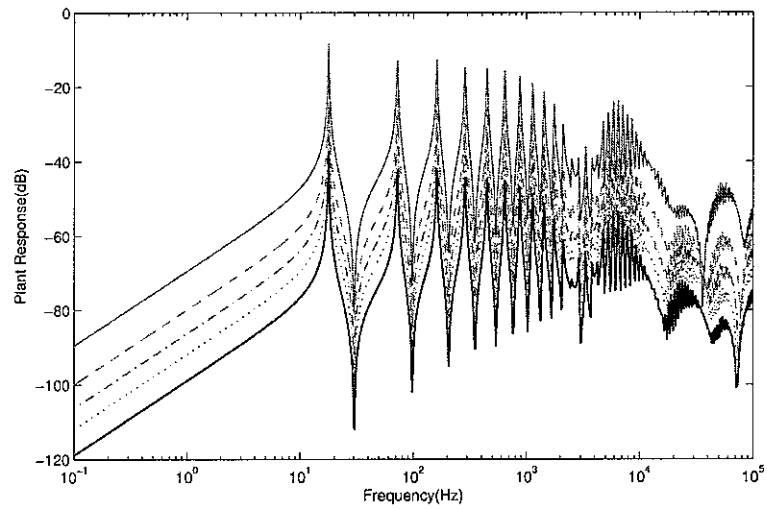


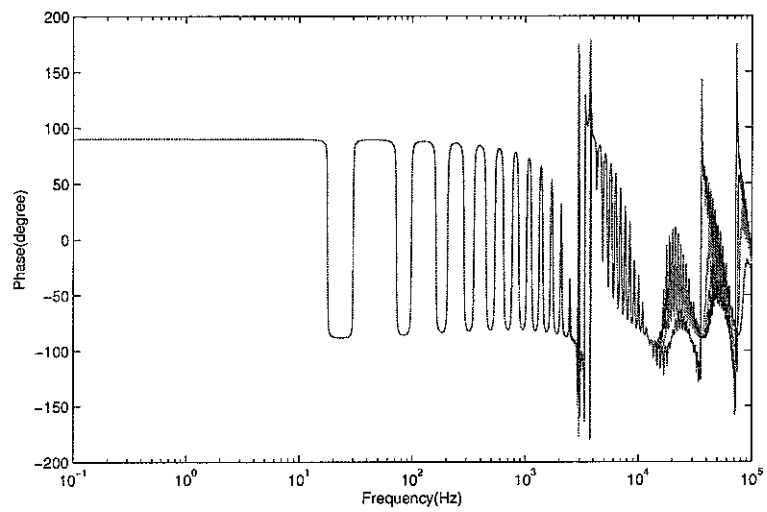
Figure 4.14: Actuator shapes varied with the top angles of $\theta_{PZT} = 15^\circ, 30^\circ, 45^\circ, 60^\circ, 75^\circ$. The boundary condition of the beam is that $\kappa = 10^5$ and $\tau = 0$.

about 26dB in this case as shown in Figure 4.16. It should be noted that the actuator with wider angle is preferable although the performance index is the same since the control effort is less. For actual beams, however, the width is limited and the height of actuator should be in the range of values such that the force generated at the vertex can couple into the beam modes up to the frequency of interest and the sensor at the vertex can respond.

The effect of the actuator's height is now examined with three different sizes of actuator with the same top angle having $\theta_{PZT} = 37^\circ$ and the height of 5mm, 10mm and 20mm as shown in Figure 4.17. The plant responses are shown in Figure 4.18. The response increases as the size of actuator increases at low frequencies, but the bigger actuator leads to the instability at lower frequency. The actuator height is hence limited by the frequency where the reduction should be guaranteed. The performance index is obtained again for the actuators as shown in Figure 4.19. It can be seen that the performance index is very small when the actuator size is small, i.e. small height. This is because the force generated by the actuator at the vertex could not couple into the structure effectively while the moment generated along the base of the actuator can couple into. For further investigation of the actuator height, four different actuators as shown in Figure 4.20 is now considered. They have the same base, $b = 15\text{mm}$, but have different heights of 20mm, 50mm, 100mm and 200mm, corresponding to $\theta_{PZT} = 37^\circ, 16.5^\circ, 8.5^\circ$ and 4.3° . Figure 4.21 shows that the magnitude of the plant responses at low frequencies up to 500Hz increases as the height of the actuator increases, while it decreases up to 2kHz. This is because of the variation of the dominant actuation



(a) Magnitude(dB)



(b) Phase(degree)

Figure 4.15: Variation of the plant response with the top angles of the triangularly-shaped piezoceramic actuator. The boundary condition of the beam is that $\kappa = 10^5$ and $\tau = 0$.

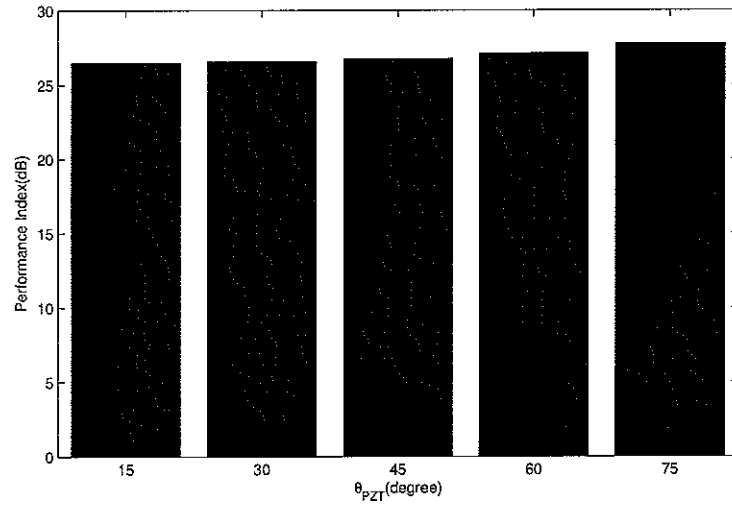


Figure 4.16: Variation of the performance index with top angles of the triangularly-shaped piezoceramic actuator. The boundary condition of the beam is that $\kappa = 10^5$ and $\tau = 0$.

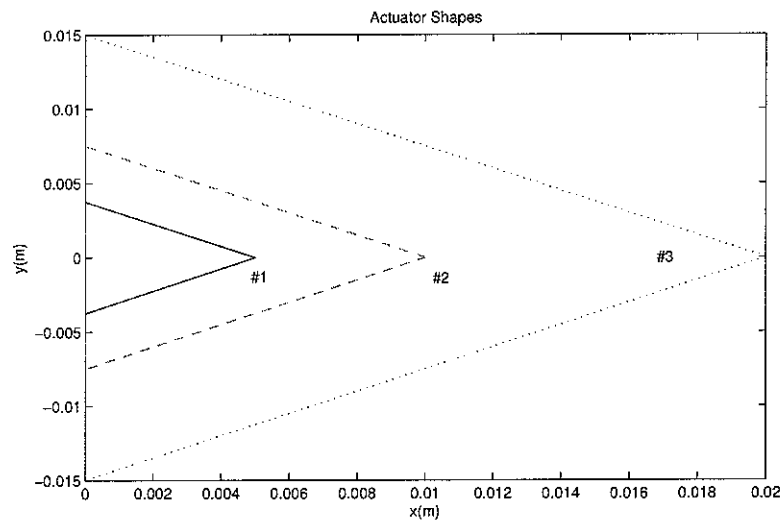
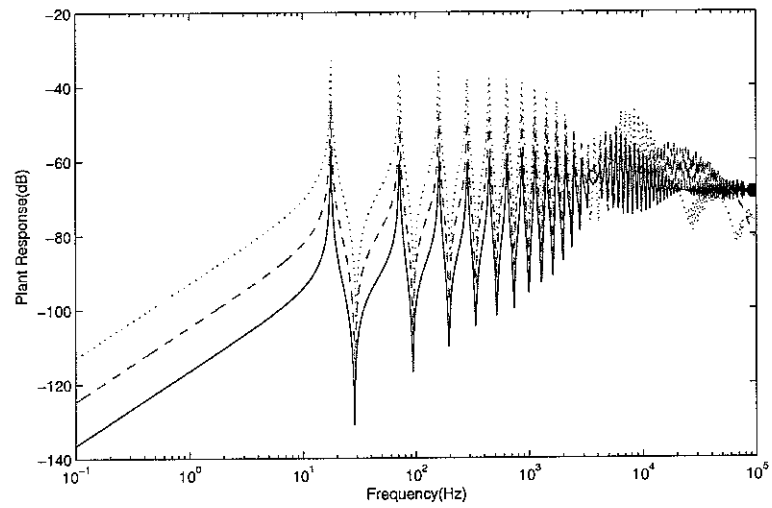
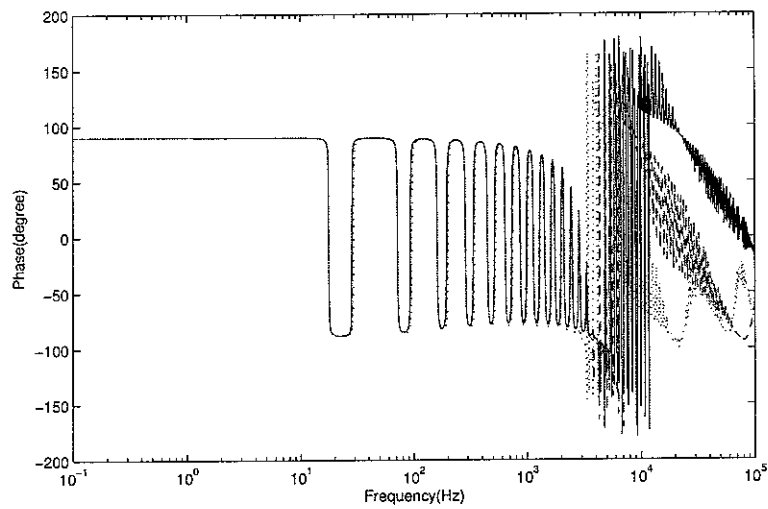


Figure 4.17: Three different sizes of the actuators with the same shapes having $\theta_{PZT} = 37^\circ$ and the height of 5mm, 10mm and 20mm. The boundary condition of the beam is that $\kappa = 10^5$ and $\tau = 0$.



(a) Magnitude(dB)



(b) Phase(degree)

Figure 4.18: Variation of the plant response with the sizes of the triangularly-shaped piezoceramic actuator. The boundary condition of the beam is that $\kappa = 10^5$ and $\tau = 0$.

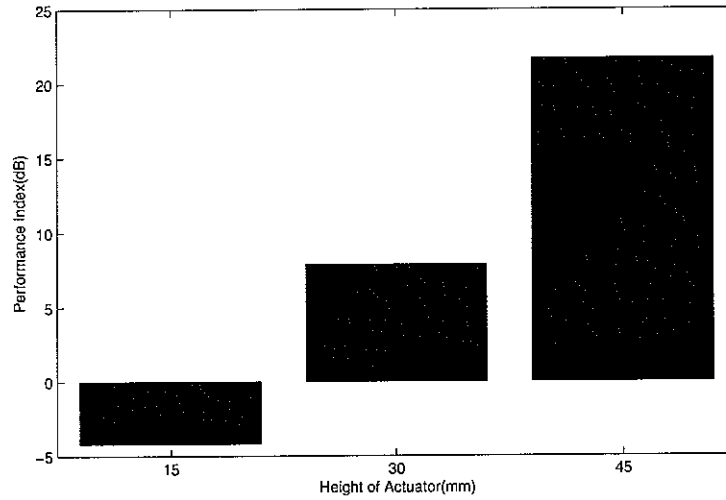


Figure 4.19: Variation of the performance index with the size of the triangularly-shaped piezoceramic actuator. The boundary condition of the beam is that $\kappa = 10^5$ and $\tau = 0$.

between the force and moment generated by the actuator for a given height. Another important feature is the cut-off frequency where the phase lag exceeding -90° occurs. This frequency decreases as the height of the actuator increases. For the case considered here, those frequencies are at 4kHz, 3kHz, 2kHz and 800Hz. The variation of the performance index shown in Figure 4.22 with the different height of actuator reflects all these behaviours. When the actuator is too small, the force does not couple into the modes efficiently so that the performance index is rather low. When the actuator is too large, the phase shift occurs at rather low frequency so that the performance index becomes relatively small.

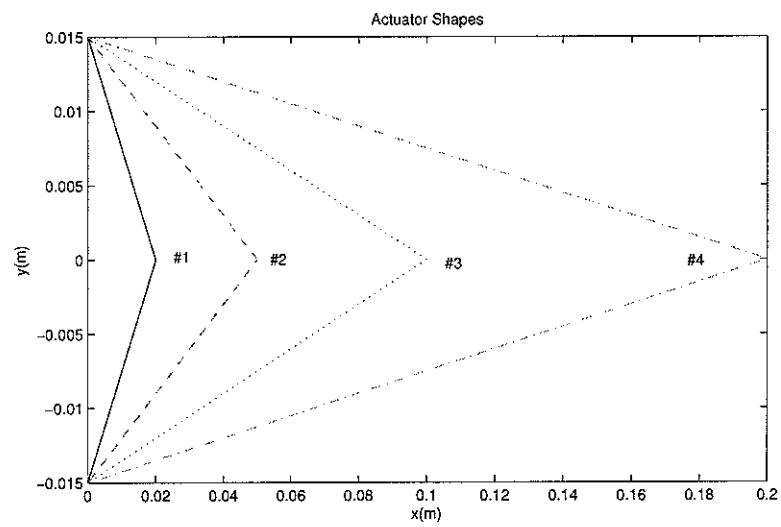
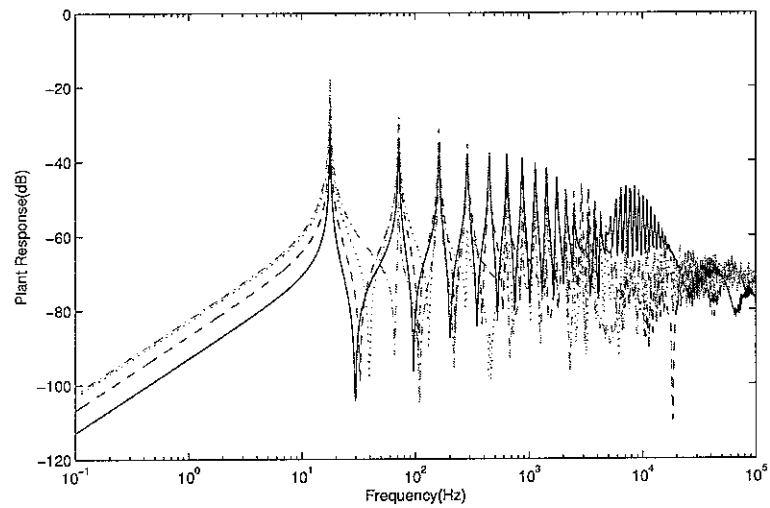
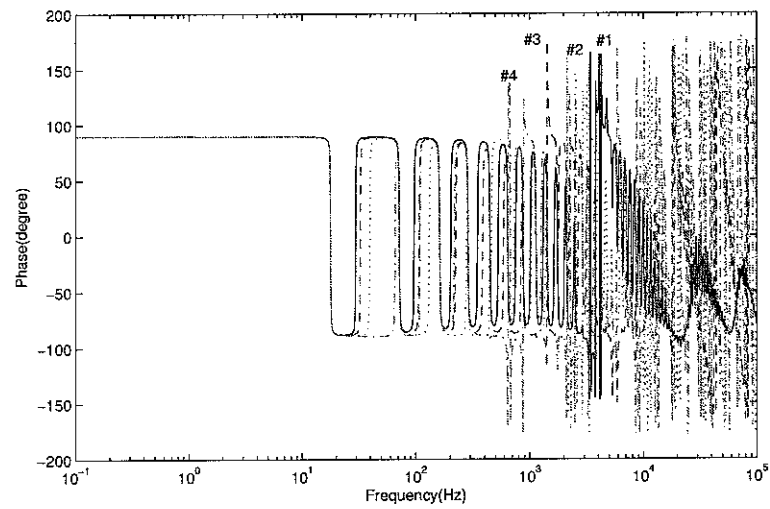


Figure 4.20: Four different shapes of the actuators having $a = 20\text{mm}$, 50mm , 100mm and 200mm with the same base of 30mm .



(a) Magnitude(dB)



(b) Phase(degree)

Figure 4.21: Variation of the plant response with the size of the triangularly-shaped piezoceramic actuator. The boundary condition of the beam is that $\kappa = 10^5$ and $\tau = 0$.

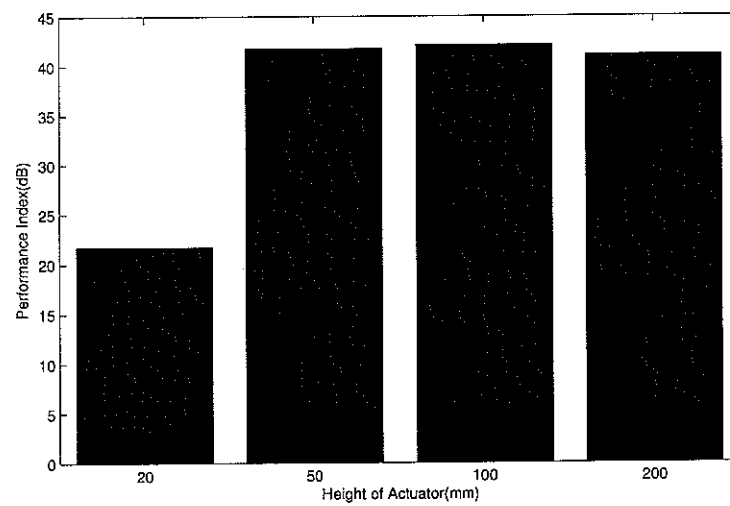


Figure 4.22: Variation of the performance index with the size of the triangularly-shaped piezoceramic actuator. The boundary condition of the beam is that $\kappa = 10^5$ and $\tau = 0$.

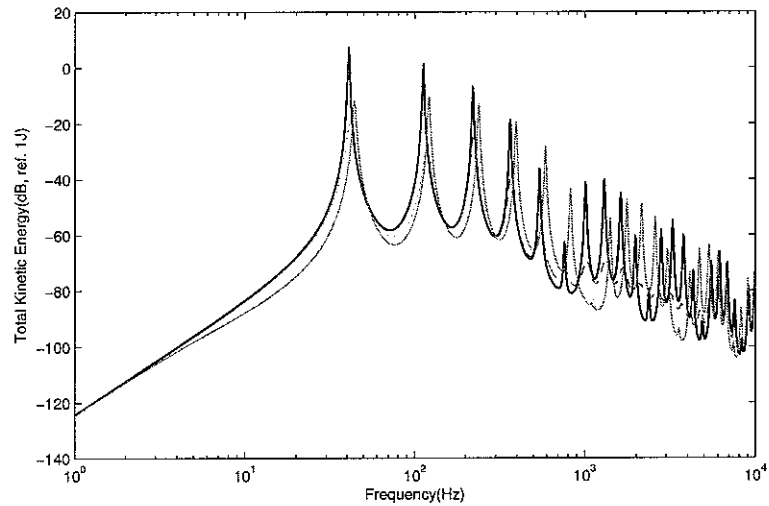
4.3 Performance

In this section the performance of the direct velocity feedback control system for beams using a triangularly-shaped piezoceramic actuators is investigated considering the beam system, shown in Figure 4.1, with only one sensor-actuator pair and a force primary excitation located at $x = 0.8L$. The effect of the boundary condition is examined first using the actuator shape of $a = 25\text{mm}$ and $b = 15\text{mm}$. The effect of actuator shape on the performance is then discussed for a resiliently-supported beam whose stiffness are $\kappa = 10^5$ and $\tau = 0$. The shapes considered here is the same combinations as considered previous section as shown in Figures 4.14, 4.17 and 4.20.

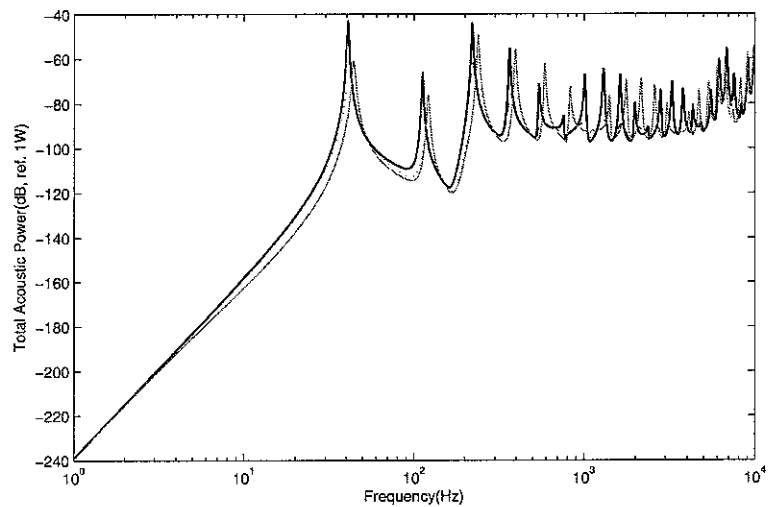
Figure 4.23 shows the performance in terms of the total kinetic energy and the acoustic power for a clamped beam excited by a concentrated force at $x = 0.2L$ and when subject to the feedback control system with gains of 10^3 , 10^4 and 10^5 . It can be seen that the total kinetic energy and the total acoustic power decrease at resonance frequencies as the feedback gain increases. Increasing the feedback gain further, however, begins to increase the response at other frequencies because the control action, which is a force in this case, is high enough to make the control point be a new boundary[18]. Therefore, the control system has a best performance at an optimal gain. Another thing to be noticed is that to obtain the same performance shown in Figure 4.24 the feedback gain is relatively higher than that for a simply supported beam. Figure 4.24 shows the control performance for a simply-supported beam under the same control system. Better performance than with the clamped beam can be achieved with a smaller feedback gain. The feedback gains used in the simulation are 100, 1000 and 2000. It should be noted that the control system for a simply supported beam is only conditionally stable. The maximum gain in this case is about 2000, which is obtained from Figure 4.3. Control spillover occurs between 5kHz and 7kHz as predicted in the plant response shown in Figure 4.3. Figure 4.25 shows the control performance of the direct velocity feedback control of a resiliently-mounted($\kappa = 10^5$ and $\tau = 0$) beam using a triangularly-shaped piezoceramic actuator($a=25\text{mm}$, $b=15\text{mm}$) with the feedback gains of 100, 300 and 600(maximum gain). The control performance is almost the same as that for simply-supported beam except for the maximum gain and the control spillover occurred between 3kHz and 4kHz.

The performance of the control systems can now be evaluated in terms of the normalised kinetic energy and acoustic power given by

$$\overline{\text{KE}}(h) = 10 \log_{10} \frac{\int_{f_1}^{f_2} \text{KE}(f, h) df}{\int_{f_1}^{f_2} \text{KE}_p(f) df}, \quad \text{dB} \quad (4.19)$$

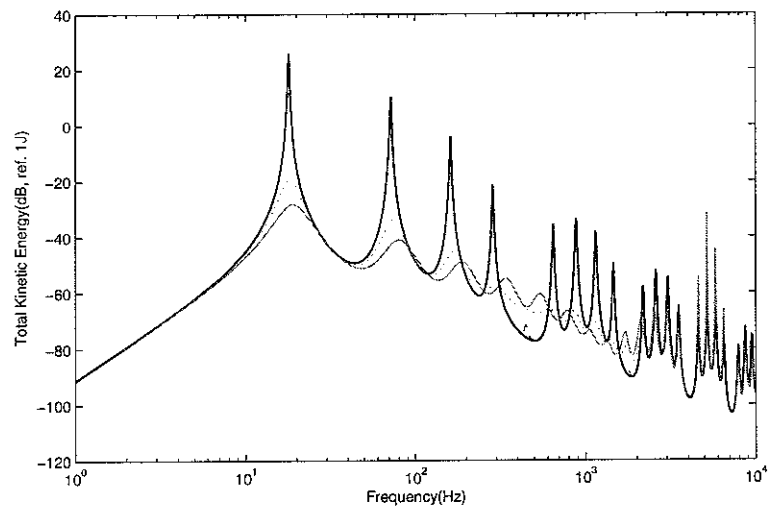


(a) Total Kinetic Energy

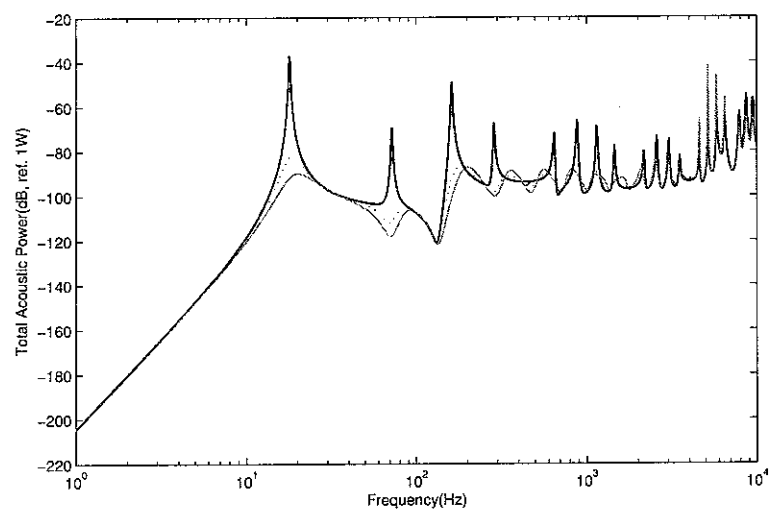


(b) Total Acoustic Power

Figure 4.23: Control performance of direct velocity feedback control of a clamped beam using a triangularly-shaped piezoceramic actuator ($a=25\text{mm}$, $b=15\text{mm}$) with the feedback gains of 10^3 , 10^4 and 10^5 .

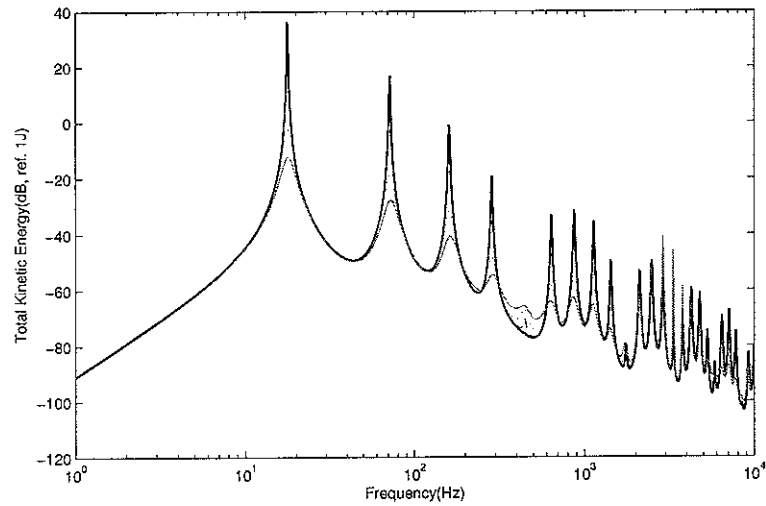


(a) Total Kinetic Energy

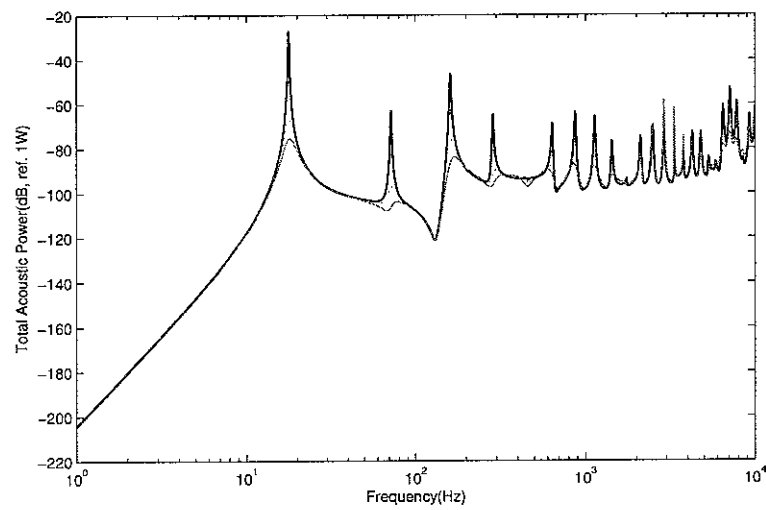


(b) Total Acoustic Power

Figure 4.24: Control performance of direct velocity feedback control of a simply supported beam using a triangularly-shaped piezoceramic actuator ($a=25\text{mm}$, $b=15\text{mm}$) with the feedback gains of 10^2 , 10^3 and 2×10^3 .



(a) Total Kinetic Energy



(b) Total Acoustic Power

Figure 4.25: Control performance of direct velocity feedback control of a resiliently-mounted ($\kappa = 10^5$ and $\tau = 0$) beam using a triangularly-shaped piezoceramic actuator ($a=25\text{mm}$, $b=15\text{mm}$) with the feedback gains of 100, 300 and 600.

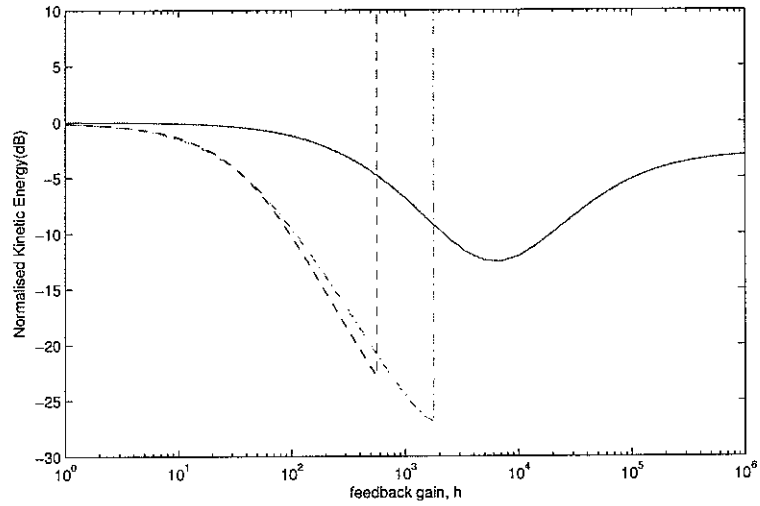
and

$$\bar{W}(h) = 10 \log_{10} \frac{\int_{f_1}^{f_2} W(f, h) df}{\int_{f_1}^{f_2} W_p(f) df}, \text{ dB} \quad (4.20)$$

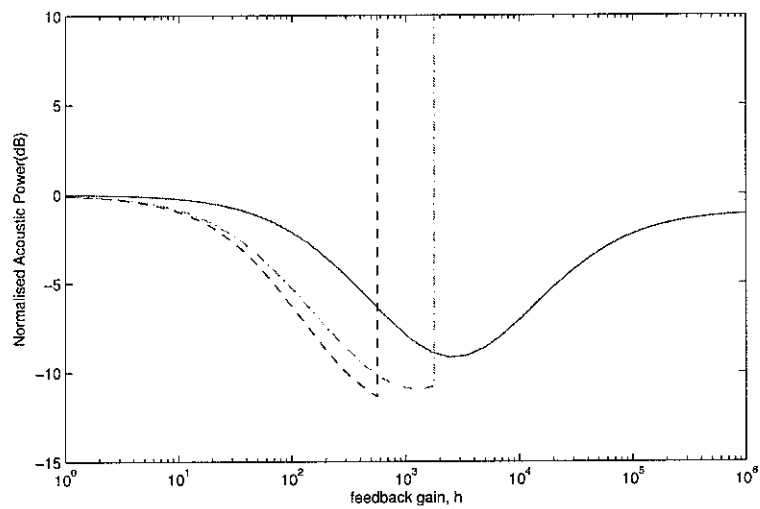
where \overline{KE} and \bar{W} represent the normalised average kinetic energy and acoustic power, respectively. Also, KE and W represent the total kinetic energy and acoustic power under the feedback control, respectively, and KE_p and W_p are those without control. f_1 and f_2 are the lower and the upper frequency of the frequency range of interest.

The normalised performance, integrated up to 1kHz, is compared in Figure 4.26 for the three boundary conditions: clamped, simply-supported and resiliently-mounted. The normalisation is performed in the frequency range between 0 and 2kHz. It can be seen that a maximum reductions of the clamped beam are restricted to 10dB in the kinetic energy and 8dB in the acoustic power by the new boundary effect of the actuator. The control system for the simply-supported beam gives much higher reduction of 25dB in the kinetic energy and 10dB in the acoustic power due to the efficient plant response. For the practical boundary condition ($\kappa = 10^5$ and $\tau = 0$), the reduction of 20dB in the kinetic energy and 11dB in the acoustic power can be achieved. It is found that the reduction in kinetic energy is brought down as the linear spring constant is lowered leading to smaller maximum gain. The reduction in the acoustic power, however, is slightly increased.

The effect of the shape of the triangular actuator on the performance of the control system implemented for the resiliently-mounted beam ($\kappa = 10^5$ and $\tau = 0$) is investigated. The variation of the shape is shown in Figures 4.14, 4.17 and 4.20. Figure 4.27 shows the effect of the actuator's top angle on the normalised control performance. With this actuator shape variation, the same reduction of 15dB in the kinetic energy and 8dB in the acoustic power can be achieved at increasing feedback gains as the width is reduced. It can be seen that the smaller top angle the actuator has, the bigger feedback gain is required to obtain the same performance. Figure 4.28 shows the effect of the actuator size with the same top angle as shown in Figure 4.17. They have the same top angle while the base and the height are increased with the same rate. It can be found that the maximum gains are almost the same, which is between 400 and 500, while the reduction performance is much different from each other. The larger actuator yields the more reduction in both the kinetic energy and the acoustic power. Finally, we considered more practical variation of the actuator shape for the beam application which are the same base of actuator having four different heights as shown in Figure 4.20. These shape combination include the variation of the top angle and the variation of the height, but note that either the top angle or the height is independent shape variable because of the constant base. The variation of the performance with the shapes

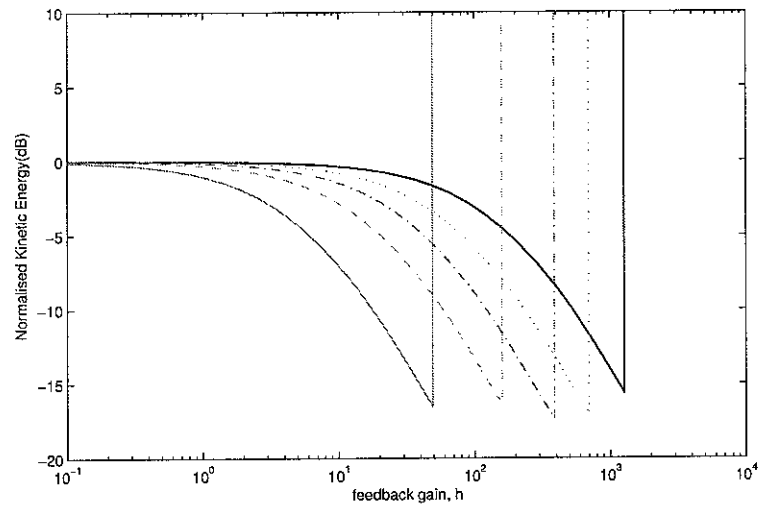


(a) Normalised Kinetic Energy

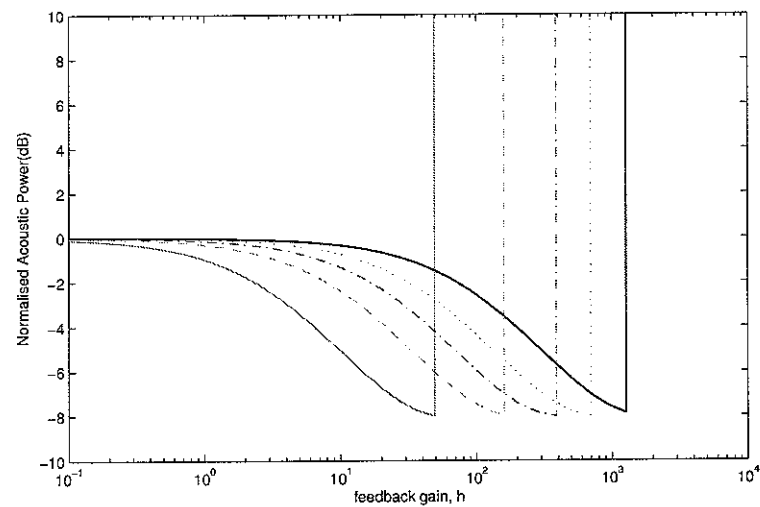


(b) Normalised Acoustic Power

Figure 4.26: Variation of the normalised control performance, integrated up to 2kHz, with the feedback gain from 1 to 10^6 for clamped beam(solid line), simply-supported beam(dot-dashed line) and resiliently-mounted beam($\kappa = 10^5$ and $\tau = 0$)(dashed line), of beams using a triangularly-shaped piezoceramic actuator($a=25\text{mm}$, $b=15\text{mm}$)

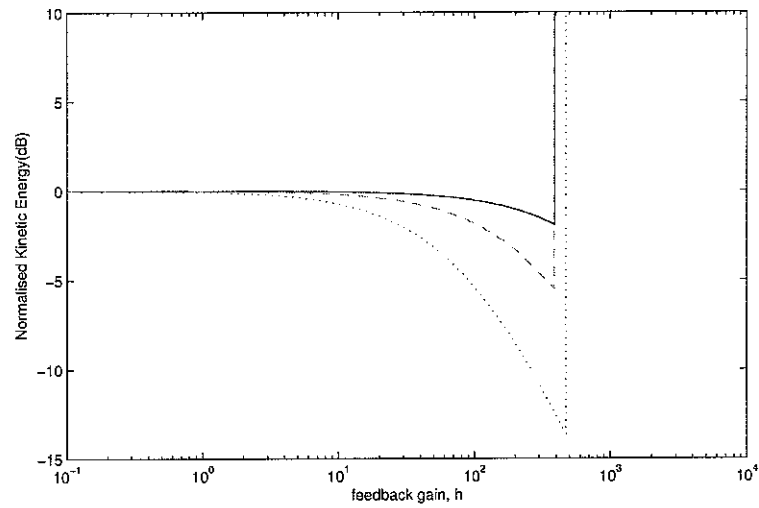


(a) Normalised Kinetic Energy

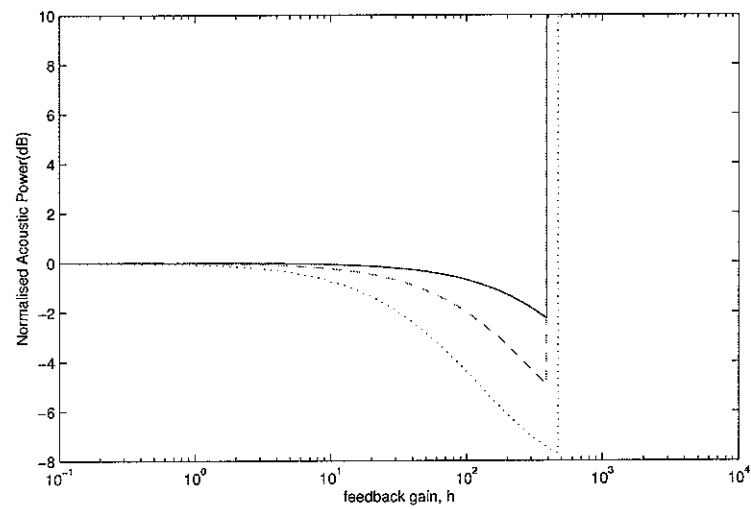


(b) Normalised Acoustic Power

Figure 4.27: Effect of the actuator's top angle on the normalised control performance with the feedback gain from 0.1 to 10^4 for the resiliently-mounted ($\kappa = 10^5$ and $\tau = 0$) beam using a triangularly-shaped piezoceramic actuator with $b=15\text{mm}$ and $\theta_{PZT} = 15^\circ$ (thick solid), $\theta_{PZT} = 30^\circ$ (dotted), $\theta_{PZT} = 45^\circ$ (dot-dashed), $\theta_{PZT} = 60^\circ$ (dashed), $\theta_{PZT} = 75^\circ$ (solid).



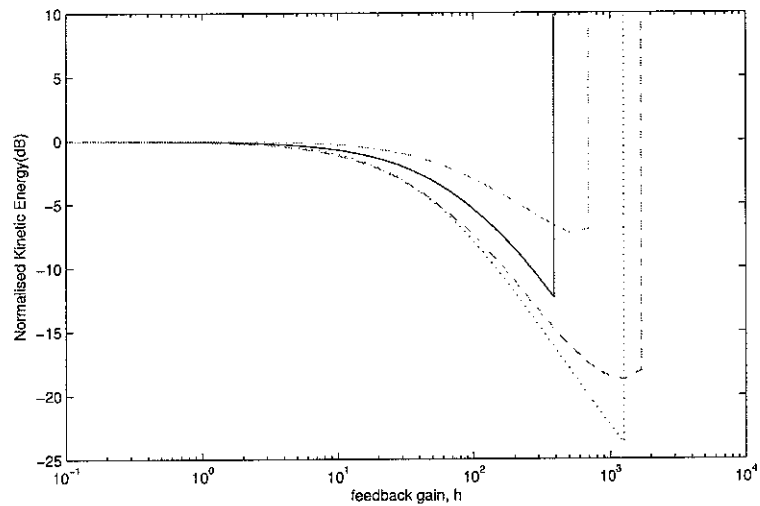
(a) Normalised Kinetic Energy



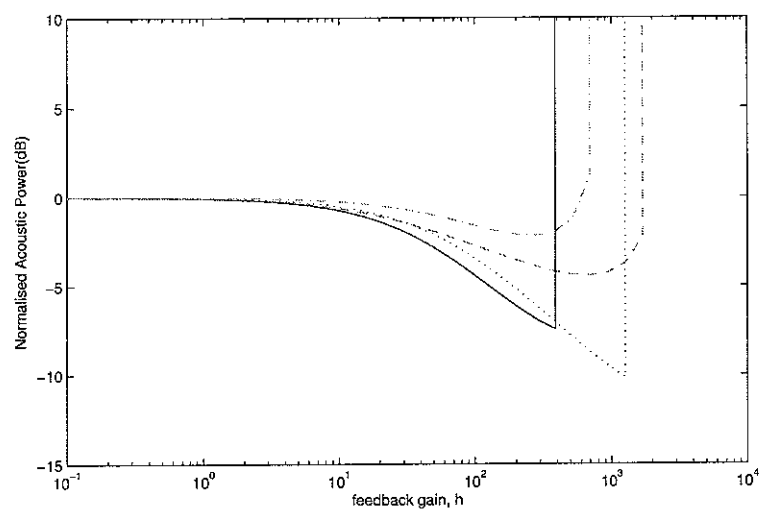
(b) Normalised Acoustic Power

Figure 4.28: Effect of the actuator shape on the normalised control performance with the feedback gain from 0.1 to 10^4 for the resiliently-mounted ($\kappa = 10^5$ and $\tau = 0$) beam using a triangularly-shaped piezoceramic actuator with $\theta_{PZT} = 37^\circ$ and $a=5\text{mm}$ (solid), 10mm (dashed) and 20mm (dotted).

are not consistent as shown in Figure 4.29. This result is the trade off of the effect of the top angle and the effect of the height. When the base is constant, the height is decreased as the top angle increased. Therefore, we can consider an optimal shape for a given base of actuator, the control purpose and the frequency range. From the four shapes of the actuator, the best performance can be achieved using the intermediate shape in the top angle and the height.



(a) Normalised Kinetic Energy



(b) Normalised Acoustic Power

Figure 4.29: Effect of the actuator shape on the normalised control performance with the feedback gain from 0.1 to 10^4 for the resiliently-mounted ($\kappa = 10^5$ and $\tau = 0$) beam using a triangularly-shaped piezoceramic actuator with $b=15\text{mm}$ and $a=20\text{mm}$ (solid), 50mm (dashed), 100mm (dotted) and 200mm (dot-dashed).

Chapter 5

Conclusions

This report is concerned with triangularly-shaped actuators for the implementation of direct velocity feedback control systems. From the general theory of the piezoceramic actuator, the excitation effects due to triangularly-shaped piezoelectric patches are derived, which consist of forces at the vertexes and moments along the edges of the actuator. The resultant actuation effect in beams is then formulated, which results in a moment and a pair of forces.

The dynamics of resiliently-mounted beam supported by both torsional and linear springs at both ends is presented and the direct velocity feedback control of the beam using the triangularly-shaped piezoceramic actuator positioned at either ends of the beam with velocity sensors at the top vertices is then implemented. It is found that the control system is influenced by the boundary condition of the beam. The shape of the actuator also affect the stability and the performance of the control system. When the beam is clamped, the triangularly-shaped actuator is perfectly collocated and dual with the velocity sensor at the tip so that the control system is unconditionally stable. In terms of performance, however, the control system for a simply-supported beam is better than for the clamped beam although the system is only conditionally stable. For practical boundary conditions achieved by the combination of the torsional and linear springs, the linear spring is essential component to effectively achieve collocation in a desired frequency range, while the torsional spring does not affect so much.

The effect of the shape of actuator is finally investigated. The bigger top angle the actuator has, the bigger is the amplitude of the plant response. With wide angled triangularly-shaped piezoactuator, the control effort can be saved. Another factor to be considered is the effect of height of the actuator. Large plant responses can be

achieved with a larger height of the actuator. The two factors, the top angle and the height, are however dependent variables such that the top angle is decreased when the height is increased. Another effect of the height is that the frequency range where stability is decreased as the height increases. It is necessary, therefore, to find the optimal dimension of the actuator for a given beam in order to maximise the control performance in the frequency range of interest.

Appendix A

Response, Kinetic Energy and Radiated Sound Power of Beams

The general solution of Equation 3.1 can be expressed as the sum of the normal modes expressed as Equations 3.17, 3.19, 3.21 or 3.23 according to the range of the spring constants. Hence, the response of the beam is written as

$$w(x, t) = \sum_{n=1}^{\infty} w_n(\omega) \phi_n(x) e^{j\omega t} \quad (\text{A.1})$$

Taking Fourier transform to Equation A.1, the total response in the function of frequency is given by

$$w(x, \omega) = \sum_{n=1}^{\infty} w_n(\omega) \phi_n(x), \quad (\text{A.2})$$

where w_n is the modal amplitude of the response. Also, the velocity distribution of the beam is represented by

$$v(x, \omega) = \sum_{n=1}^{\infty} a_n(\omega) \phi_n(x), \quad (\text{A.3})$$

where $a_n = j\omega w_n$. Substituting Equation A.1 into Equation 3.1 and employing Equation 3.25 and the orthonormal property of the normal modes, we can obtain the modal amplitude expressed by

$$a_n = A_n(\omega) F_n(\omega), \quad (\text{A.4})$$

where

$$A_n(\omega) = \frac{j\omega}{\rho AL[(1 + j\eta)\omega_n^2 - \omega^2]}, \quad (\text{A.5})$$

and A is the cross sectional area of the beam, ζ_n is the modal damping ratio, and F_n is the modal excitation term which will have a component due to the external force and the external moment, so that

$$F_n(\omega) = \int_0^L f(x, \omega) \phi(x) dx + \int_0^L \frac{\partial T(x, t)}{\partial x} \phi(x) dx. \quad (\text{A.6})$$

In Equation A.2, the velocity distribution of the beam is assumed to be a finite modal series

$$\begin{aligned} v(x, \omega) &= \sum_{n=1}^N a_n(\omega) \phi_n(x) \\ &= \mathbf{a}^T \boldsymbol{\phi}(x) \end{aligned} \quad (\text{A.7})$$

where N is the number of modes taken into account, \mathbf{a} is the vector of modal velocity amplitude, a_n , i.e;

$$\mathbf{a} = \{a_1, a_2, \dots, a_n\}^T, \quad (\text{A.8})$$

the superscript H indicates the Hermiltian transpose and $\boldsymbol{\phi}(x)$ is the vector of modes at a position x , i.e,

$$\boldsymbol{\phi}(x) = \{\phi_1(x), \phi_2(x), \dots, \phi_N(x)\}^T. \quad (\text{A.9})$$

The total kinetic energy of the beam is defined to be

$$E(\omega) = \frac{\rho A}{2} \int_0^L |v(x, \omega)|^2 dx. \quad (\text{A.10})$$

Introducing Equation A.7 and orthonormal property of the modes shown in Equation 3.25 into Equation A.10, the kinetic energy can be expressed by

$$E(\omega) = \frac{\rho A}{4L} \mathbf{a}^H \mathbf{a}. \quad (\text{A.11})$$

Assuming the beam is in an infinite rigid baffle, the sound power radiated by the beam is calculated using Cunefare[19]. When the velocity distribution on the beam is expressed by Equation A.7 and the modal velocity amplitude vector is available, the sound radiated power from the infinitely baffled beam can be expressed by

$$W = \mathbf{a}^H \mathbf{M} \mathbf{a}, \quad (\text{A.12})$$

where \mathbf{M} is the *modal* radiation resistance matrix in which the diagonal terms are self-

radiation resistances and the off-diagonal terms are the mutual-radiation resistances. The numerical values of the elements of them matrix \mathbf{M} have been calculated, for example by Cunefare[19] and Baumann, *et al* [20], by integrating the far-field pressure. Also, Elliott, *et al*[21] presented a method of calculating the matrix by considering a number of elemental radiators. In this study, we summarised their work and used to calculate the matrix \mathbf{M} . If the vector of complex linear velocities, \mathbf{v} , of each of these elemental radiators is given, the sound pressure immediately in front of each source \mathbf{p} is written by

$$\mathbf{p} = \mathbf{Z}\mathbf{v} \quad (\text{A.13})$$

where \mathbf{Z} is a matrix of specific acoustic impedances which is symmetric so that $\mathbf{Z} = \mathbf{Z}^T$. Since the acoustic power radiated by this array of elemental sources is proportional to the real part of the sum of the conjugate volume velocities of each radiator multiplied by the corresponding acoustic pressure, the acoustic power is

$$W = \frac{S}{2} \text{Re}(\mathbf{v}^H \mathbf{p}), \quad (\text{A.14})$$

where S is the area of the radiators which are assume to be same size, for convenience. Using Equation A.13, Equation A.14 can be rewritten as

$$\begin{aligned} W &= \frac{S}{2} \text{Re}[\mathbf{v}^H \mathbf{Z}\mathbf{v}] \\ &= \frac{S}{4} \text{Re}[\mathbf{v}^H (\mathbf{Z}^H + \mathbf{Z})\mathbf{v}] \\ &= \mathbf{v}^H \mathbf{R}\mathbf{v} \end{aligned} \quad (\text{A.15})$$

where $\mathbf{R} = (S/2)\text{Re}(\mathbf{Z})$ expressed of the form

$$\mathbf{R} = \frac{\omega^2 \rho S^2}{4\pi c} \begin{bmatrix} 1 & \frac{\sin(kr_{12})}{kr_{12}} & \dots & \frac{\sin(kr_{1I})}{kr_{1I}} \\ \frac{\sin(kr_{21})}{kr_{21}} & 1 & \dots & \vdots \\ \vdots & \vdots & \dots & \vdots \\ \frac{\sin(kr_{I1})}{kr_{I1}} & & & 1 \end{bmatrix} \quad (\text{A.16})$$

But, \mathbf{v} can be expressed as

$$\mathbf{v} = \Phi \mathbf{a}, \quad (\text{A.17})$$

where Φ is $I \times N$ matrix of the discretised mode shape. Hence, the radiated acoustic power is, using Equation A.15 and A.17, written as

$$W = \mathbf{a}^H \Phi^H \mathbf{R} \Phi \mathbf{a}. \quad (\text{A.18})$$

It is noted that the accuracy of the estimated radiated power will increase with the number of elemental radiators considered (I). Comparing equation (A.35) with Equation A.12, the modal radiation resistance matrix should be

$$\mathbf{M} = \mathbf{\Phi}^H \mathbf{R} \mathbf{\Phi}. \quad (\text{A.19})$$

Since the radiation matrix \mathbf{R} is given as Equation A.16, we can easily calculate the modal radiation resistance matrix \mathbf{R} and then the acoustic power expressed as Equation A.12. In this study, the kinetic energy and radiated acoustic power are used as a cost function for optimisation. Also, they are used to estimate the performance of the noise control. The radiation efficiency is useful for evaluating the physical characteristics of control performance. The radiation efficiency is generally defined as

$$\sigma = W / \rho c S_T \langle \overline{u^2(t)} \rangle \quad (\text{A.20})$$

where S_T is the total radiating area of the beam and $\langle \overline{u^2(t)} \rangle$ is its space average mean-square velocity. Introducing Equations A.18, A.19 and $\langle \overline{u^2(t)} \rangle = \mathbf{a}^H \mathbf{a} / 2$ into A.20, the radiation efficiency can be written as

$$\sigma_{ij} = 2M_{ij} / \rho c S_T \quad (\text{A.21})$$

Equation A.21 can be expressed in the matrix form as

$$\Sigma = 2\mathbf{M} / \rho c S_T, \quad (\text{A.22})$$

whose diagonal elements are the radiation efficiencies of each structural modes alone, which is called the normalised self-radiation efficiencies, and whose off-diagonal elements are the normalised mutual-radiation efficiencies.

References

- [1] F. J. Fahy, *Sound and Structural Vibration*. Academic Press, London, 1994.
- [2] P. Gardonio and S. J. Elliott, "Smart panels with velocity feedback control systems using triangularly shaped strain actuators," *Journal of Acoustical Society of America*, vol. 117, April 2005.
- [3] S. J. Elliott, P. Gardonio, T. C. Sors, and M. Brennan, "Active vibroacoustic control with multiple local feedback loops," *Journal of Acoustical Society of America*, pp. 908–915, 2002.
- [4] P. Gardonio, E. Bianchi, and S. J. Elliott, "Smart panel with multiple decentralized units for the control of sound transmission. part i. theoretical predictions," *Journal of Sound and Vibration*, vol. 274, pp. 163–192, 2004.
- [5] P. Gardonio, E. Bianchi, and S. J. Elliott, "Smart panel with multiple decentralized units for the control of sound transmission. part ii. design of decentralized control units," *Journal of Sound and Vibration*, vol. 274, pp. 193–213, 2004.
- [6] E. Bianchi, P. Gardonio, and S. J. Elliott, "Smart panel with multiple decentralized units for the control of sound transmission. part iii. control system implementation," *Journal of Sound and Vibration*, vol. 274, pp. 215–232, 2004.
- [7] C. K. Lee, "Theory of laminated piezoelectric plates for the design of distributed sensors/actuators. part i. governing equations and reciprocal relationships," *Journal of Acoustical Society of America*, vol. 87, pp. 1144–1158, March 1990.
- [8] J. M. Sullivan, J. J. E. Hubbard, and S. E. Burke, "Distributed sensor/actuator design for plates: Spatial shape and shading as design parameters," *Journal of Sound and Vibration*, vol. 203, no. 3, pp. 473–493, 1997.
- [9] S. J. Elliott, P. Gardonio, T. C. Sors, and M. J. Brennan, "Active vibroacoustic control with multiple local feedback loops," *The Journal of the Acoustical Society*

- of America - February 2002 - Volume 111, Issue 2, pp. 908-915, vol. 111(2), pp. 908-915, 2002.*
- [10] J. M. Sullivan, J. James E. Hubbard, and S. E. Burke, "Modeling approach for two-dimensional distributed transducers of arbitrary spatial distribution," *Journal of Acoustical Society of America*, vol. 99, pp. 2965-2974, May 1996.
- [11] S. S. Rao, *Mechanical Vibrations*. Addison-Wesley Publishing Company, Inc., 1970.
- [12] E. B. Magrab, *Vibrations of Elastic Structural Members*. Sijthoff and Noordhoff International Publishers B.V., 1979.
- [13] S. E. Burke and J. James E. Hubbard, "Active vibration control of a simply supported beam using a spatially distributed actuator," *IEEE Control Systems Magazine*, pp. 25-30, 1987.
- [14] L. Meirovitch, ed., *Observability of a Bernoulli-Euler Beam Using PVF₂ as a Distributed Sensor*, (VPI&SU, Blacksburg, VA), 1987.
- [15] Y.-S. Lee, S. J. Elliott, and P. Gardonio, "Matched piezoelectric double sensor/actuator pairs for beam control," *Smart Materials and Structures*, vol. 12, pp. 541-548, 2003.
- [16] G. F. Franklin, J. D. Powell, and A. Emami-Naeini, *Feedback Control of Dynamic Systems(2nd. Ed.)*. Addison-Wesley Publishing Company, Inc., 1991.
- [17] C. Hong, *Active control of a resiliently-mounted flexible structures*. PhD thesis, Institute of Sound and Vibration, University of Southampton, 2005.
- [18] P. Gardonio and S. J. Elliott, "Modal response of a beam with a sensor-actuator pair for implementation of velocity feedback control," *Journal of sound and vibration*, vol. 284, pp. 1-22, 2005.
- [19] K. A. Cunefare, "The minimum multimodal radiation efficiency of baffled finite beams," *Journal of Acoustic Society of America*, vol. 90, pp. 2521-2529, 1991.
- [20] W. T. Baumann, W. R. Saunders, and H. R. Robertshaw, "Active suppression of acoustic radiation from impulsively excited structures," *Journal of Acoustic Society of America*, vol. 90, pp. 3202-3208, 1991.
- [21] S. J. Elliott and M. E. Johnson, "Radiation modes and the active control of sound power," *Journal of Acoustical Society of America*, pp. 2194-2204, 1993.